



**HAL**  
open science

# LES investigation of cycle-to-cycle variation in a SI optical access engine using TFM-AMR combustion model

Jacopo Zembi, Michele Battistoni, Suresh Kumar Nambully, Adrian Pandal, Cédric Mehl, Olivier Colin

► **To cite this version:**

Jacopo Zembi, Michele Battistoni, Suresh Kumar Nambully, Adrian Pandal, Cédric Mehl, et al.. LES investigation of cycle-to-cycle variation in a SI optical access engine using TFM-AMR combustion model. International Journal of Engine Research, 2022, 23 (6), pp.1027-1046. 10.1177/14680874211005050 . hal-03994389

**HAL Id: hal-03994389**

**<https://ifp.hal.science/hal-03994389>**

Submitted on 14 Mar 2023

**HAL** is a multi-disciplinary open access archive for the deposit and dissemination of scientific research documents, whether they are published or not. The documents may come from teaching and research institutions in France or abroad, or from public or private research centers.

L'archive ouverte pluridisciplinaire **HAL**, est destinée au dépôt et à la diffusion de documents scientifiques de niveau recherche, publiés ou non, émanant des établissements d'enseignement et de recherche français ou étrangers, des laboratoires publics ou privés.

# LES Investigation of Cycle-to-Cycle Variation in a SI Optical Access Engine using TFM-AMR Combustion Model

Zembi Jacopo<sup>1</sup>, Michele Battistoni<sup>1</sup>, Suresh Kumar Nambully<sup>2</sup>, Adrian Pandal<sup>3</sup>, Cédric Mehl<sup>4</sup>, Olivier Colin<sup>4</sup>

*1 Università degli Studi di Perugia, Department of Engineering, Italy*

*2 Convergent Science GmbH, Austria*

*3 Universidad de Oviedo, Spain*

*4 IFP Energies Nouvelles, France*

## ABSTRACT

Multi-cycle large-eddy simulations (LES) are performed to investigate combustion cycle-to-cycle variability (CCV) in a gasoline spark ignited optical access engine operating under homogeneous stoichiometric conditions. Combustion is addressed with the Thickened Flame Model (TFM) and finite rate chemistry is accounted for through a reduced oxidation reaction mechanism. In view of the fact that computational costs of LES engine simulations are still very high today, this work investigates the use of adaptive mesh refinement (AMR) in the flame zone in conjunction with the artificial flame thickening applied by the TFM model. The paper discusses how the resulting coupled TFM-AMR combustion model allows good resolution of the flame, maintaining accuracy at acceptable costs. First, the details of the coupled model are presented and the effects of the parameters are explored, highlighting their impact on the combustion prediction. Then, computational fluid dynamics (CFD) simulation results are validated against experimental data collected in a low-speed low-load engine point, by comparing 20 LES cycles and 100 measured cycles, for mass fraction burned, combustion phasing, flame images and CCV indices. Lastly, a detailed investigation on the fastest and slowest numerical cycles is presented, analyzing instantaneous flame structures, ignition behaviors, propagation speeds, and probability density function (PDF) of the instantaneous velocity fluctuation around the spark region. The results show that combustion variability is highly correlated to the resolved velocity field and the resolved turbulence intensity, which is found to be the main cause of CCV and affects the early flame kernel growth. This work is an early attempt to use TFM-AMR combustion model for LES simulations of internal combustion engines.

## A. INTRODUCTION

Over the last decades, the internal combustion engine (ICE) research community and manufacturers have been investing very large amount of resources in order to reduce emission levels and increase thermal efficiency of internal combustion engines [1]. But, recently, also hybrid (HEV) or electric vehicles (EV) [2, 3] have drawn much attention and resources. The competing technologies will contribute to keep pushing the boundaries of all available technologies, considering the fact that even the more optimistic scenarios for decarbonizing the transportation sector still foresee dominance of energy coming from liquid fuels worldwide up to 2040 [4]. In this context, reducing pollutant and CO<sub>2</sub> emissions of ICE is even more urgent and needed for their wide impact, also because of their relatively cheap but sophisticated technology.

Promising and advanced technological solutions have been suggested and explored to reach clean and efficient combustion in spark ignition (SI) engines, such as engine downsizing [5], direct-injection with charge stratification [6], lean mixture operation [7, 8], controlled auto-ignition [9, 10], water injection [11, 12, 13, 14], exhaust gas recirculation [15, 16]. Innovative ignition strategies have been also proposed and explored, like plasma assisted ignition systems [17, 18] or pre-chamber turbulent jet ignition [19, 20, 21], homogeneous charge compression ignition (HCCI) [22, 23] and reactivity controlled compression ignition (RCCI) [24, 25]. These advanced combustion concepts can improve engine efficiency by 10-20% [26, 4] and simultaneously reduce pollutant emissions [27, 28]. However, the operational range of such concepts can be significantly limited by cycle-to-cycle variability (CCV).

CCV is defined as the non-repeatability of combustion process from one cycle to another for nominal constant operating conditions [29]. CCV is undesirable since it has adverse effects on combustion stability, emissions and efficiency, it leads to sub-optimal designs and calibrations, and it can affect engine components durability and vehicle drivability. In fact, CCV is the result of a complex combination of different flow phenomena. The

origins of CCV can be grouped into two categories: (i) deterministic, due to the feedback effect of the previous cycles [30]; (ii) stochastic, due to the intrinsically turbulent nature of the flow field. Various causes of CCV have been investigated [31]: cylinder charge motions variations, turbulence characteristics variations, inhomogeneity of the mixture [32, 33] and residual burnt gases [34]. For spark ignited engines, which are the focus of the present study, particular attention must be paid to the region near the spark plug before the time of ignition [35] where the local flow features can affect the initial size of the flame kernel. Studies dealing with LES in motored piston engines are numerous, and various reactive LES of SI engines which aim at reproducing CCV can be found in the literature.

Recent works [36, 37, 38, 39, 40] proved the ability of LES to capture CCV. Vermorel et al. [41] have applied LES models developed by Richard et al. [42] to explore the origins of CCV investigating 10 consecutive LES cycles in a single cylinder SI engine. They showed that the major sources of cyclic variabilities are derived from the variation in tumble motion, produced during the intake stroke, and from the high turbulence intensity around the ignition timing. Overall or local mixture variations did not have a significant influence on the CCV generation. Granet et al. [43] simulated 25 consecutive cycles of a stable and 50 cycles of an unstable operating engine point demonstrating the capability of LES to satisfactorily predict experimentally observed CCV levels. Furthermore, the causes of incomplete combustion occurred in some cycles of the high CCV case were investigated through a qualitative analysis of the LES. Enaux et al. [44] carried out an LES study in a propane-fueled SI engine suggesting that CCV causes are mainly due to fluctuations in the velocity field around the spark region, which produce variations of the early flame kernel growth and, consequently, of the overall combustion process. LES ability to reproduce the characteristics of turbulent flow structures [45, 46, 47, 48] and of turbulent combustion [49, 50, 51, 52] in SI engines is also found in the literature. Truffin et al. [53] suggested that the causes of CCV lie on the effect of convection flow at the spark plug, as well as on the type of engine and its operating conditions. The work by Thobois et al. [54] showed that LES is intrinsically able to reproduce combustion CCV on single-cylinder internal combustion engines (ICEs) using both Thickened Flame Model (TFM) [55] and Extended Coherent Flame Model (ECFM) [56, 57]. Fontanesi et al. [58, 59] performed LES analysis of 20 cycles, optimizing grid size, grid distribution and numerical settings to achieve a balance between simulation accuracy and computational time. They found that the conditions around the spark (inhomogeneity and variation in fuel distribution, turbulent energy and velocity magnitude) are the primary factors contributing to CCV. Zhao et al., [60] and Truffin et al., [53], conducted some interesting studies on the effect of specific flow variables around the spark gap, just prior-to-ignition, and found that changes in the velocity field are responsible for large differences in flame propagation, while variations in the local equivalence ratio field are less impactful.

In the LES framework, two problems arise for the simulation of premixed flames [55]. First of all, the typical LES meshes are not refined enough to resolve the laminar flame thickness. Moreover, interactions between unresolved turbulent structures and flame front must be modeled. The TFM combustion model [61] has been proposed to address these aspects. The flame front is artificially thickened and the interaction between the small scale turbulent structures and the flame is modeled via a subgrid-scale (SGS) wrinkling factor [61, 62], accounting for the increased flame propagation speed due to unresolved flame wrinkling. An additional advantage of the TFM is that it can be coupled with detailed or reduced chemistry, as applied in this work, to predict also emissions, knock or other phenomena where accurate representation of turbulence-chemistry interaction is essential.

In addition, LES simulations of most engineering devices are still today challenging because of the computational costs involved. Even if the resolution of a typical LES mesh can be fine enough for resolving 80-90% of the kinetic energy associated with the flow, it might still be one or two orders of magnitude larger than the laminar flame thickness. Flame thickening alone cannot cover such large range accurately. In such cases, adaptive mesh refinements (AMR) on the flame region can substantially improve the calculation accuracy and the computational efficiency, thus reducing the overall cost. A coupling between AMR and TFM has been proposed in [63], in the context of laboratory flames, providing a very efficient use of AMR while keeping the cell resolution high enough inside the flame, thanks to thickening.

This work, to the best of the authors' knowledge, is an early attempt to use TFM-AMR combustion model in the engine community. We investigate a low-speed low-load SI engine case with low levels of turbulence; the flame is resolved by introducing AMR in the reactive layers, combined with the thickened flame combustion model. The coupled TFM-AMR approach is found to be suitable for a detailed analysis of the investigated

conditions and for reducing the overall computational cost. The objective of this study is to propose a methodology to investigate CCV sources in spark ignition engines, using TFM-AMR combustion model in a LES framework.

The work is organized in the following manner. Experimental and numerical setups are presented in Sec. B and C. An exploration of TFM combustion model and TFM-AMR coupling is carried out in Sec. D and E. Results of LES simulations and comparisons between numerical and experimental data are discussed in Sec. F. Main conclusions and some perspectives for future work are outlined in Sec. G.

## B. OPTICAL ACCESS SI ENGINE SETUP

The optical engine, shown in Figure 1, is a 500 cm<sup>3</sup> single cylinder engine with a pent-roof combustion chamber, four valves and reverse tumble intake port design. It can be operated in Direct Injection (DI) or in Port Fuel Injection (PFI) mode, which is the case in this study. The combustion chamber is optically accessible through a 60 mm diameter quartz piston crown window, in conjunction with an extended piston and a stationary 45-degree mirror [64]. Graphite rings are used to avoid lubricant presence in the combustion chamber, maintaining the quartz window clean. A regular European gasoline with RON 95 MON 85 is used as the fuel [65, 66].

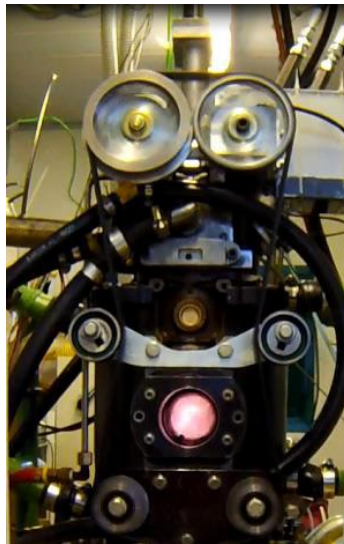


*Figure 1. Optical access engine in firing condition.*

The main engine features are given in Table 1. Engine operation is controlled in terms of speed, air-flow, injection and ignition start. Speed control is obtained using an AVL 5700 dynamic brake, coupled to the optical engine. Load regulation is achieved by adjusting the PFI injection duration, while the throttle valve is maintained at a fixed position, to ensure constant airflow and tumble motion. The air-fuel ratio is controlled by a dedicated ECU regulating the injected fuel mass. The stoichiometric condition at 1000 rpm and ~5 bar brake mean effective pressure (BMEP) is considered in this study. The ignition timing is then adjusted for the maximum brake torque value. A piezoresistive transducer (Kistler 4075A5) at the intake measures the intake port pressure and a piezoelectric transducer (Kistler 6061 B) installed on one side of the chamber measures the in-cylinder pressure. An optical encoder with 0.1 CAD resolution is used to reference the pressure signals to the angular position of the crankshaft. In the investigated operating point, 100 consecutive cycles are recorded and post-processed. A Vision Research Phantom V710 high-speed CMOS camera coupled with a Nikon 55 mm f/2.8 lens is used to record natural luminosity flame images. The sampling rate is 20 kHz, corresponding to 0.3 CAD at 1000 rpm. 63 consecutive combustion events are recorded collecting images in sync with the indicated pressure. The experimental methodology and results have been presented elsewhere [67, 68].

Table 1. Engine data and operating conditions.

Displacement	500 cm <sup>3</sup>
Bore	0.085 m
Stroke	0.088 m
Connecting rod length	0.139 m
Compression ratio	8.8:1
Number of valves	4
Engine speed	1000 rpm
Indicated Mean Effective Pressure	~5 bar @ $\lambda=1$
Intake valve open	329 CAD aTDC
Intake valve close	547 CAD aTDC
Exhaust valve open	170 CAD aTDC
Exhaust valve close	380 CAD aTDC
Fuel	Standard European market Gasoline, RON 95 MON 85
Injection	PFI
Lambda	1.0
Spark ignition timing	-20 CAD aTDC

### C. COMPUTATIONAL SETUP

CONVERGE v3.0.11 CFD solver [69, 70] is used as the computational framework for this study. Figure 2-left shows the domain used for the simulations. The grey region is the plenum, in blue is the throttle body, the green region is the intake port, in red is the combustion chamber and the yellow region is the exhaust port. The code performs the calculation of the three-dimensional, compressible, chemically-reacting flows in complex geometries with moving boundaries, and it is specifically tailored for piston engine analysis. The code automates the mesh generation process very efficiently using a Cartesian orthogonal grid and a cut-cell method at the boundaries, with various adaptive and prescribed methods for managing refinements. (Figure 2-right).

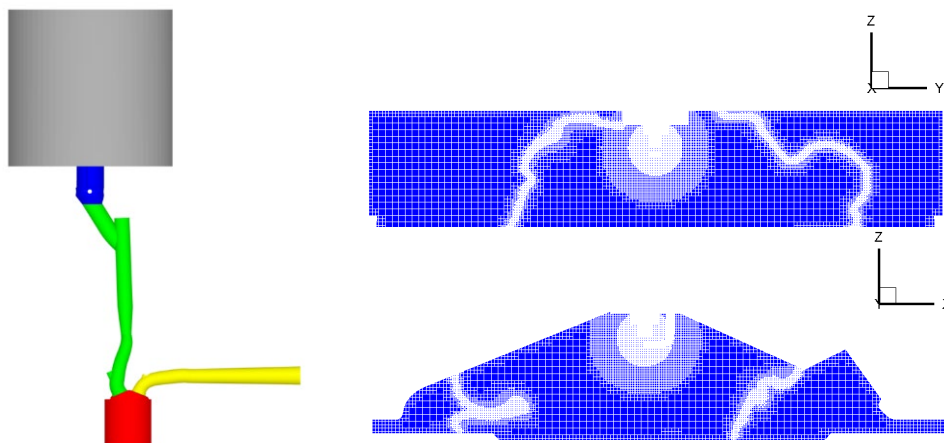


Figure 2. CFD engine model: simulation domain (left), mesh (right).

The finite volume method is used to solve the overall set of compressible Favre-filtered Navier-Stokes, species and energy equations. Conservation of mass and momentum are solved via a pressure-velocity coupling algorithm, using the Pressure Implicit with Splitting of Operators (PISO) method [71]. A second-order spatial discretization scheme is used for the governing conservation equations. The time-step is automatically calculated during each computational step based on maximum allowed Courant-Friedrichs-Levy (CFL) numbers for convection. Turbulence is modeled using the Dynamic Structure Model [72] for Large Eddy Simulations.

As already mentioned, the TFM-AMR combustion model is used, and its theoretical overview will be specifically discussed in Sec. D. One key point of this combustion model is that it is coupled to chemical kinetics for the prediction of the reaction source terms and hence flame propagation. Here, gasoline chemical kinetics has been considered using a reduced mechanism [73] for primary reference fuels (PRF), i.e., iso-octane

and n-heptane, consisting of 110 species and 488 reactions derived from a Lawrence Livermore National Laboratory detailed mechanism. To model gasoline combustion a fuel surrogate representation of 95% iso-octane and 5% n-heptane by volume is used. Fuel injection is not modeled, but fuel and air are considered to be perfectly mixed at the inflow boundary. Note that in the present perfectly premixed indirect injection configuration, the port fuel injector is positioned at the beginning of the intake duct (upper part of green boundary in Figure 2-left), therefore other sources as mixture heterogeneities or interactions between fuel spray and aerodynamics can be neglected as CCV sources (as shown by Richard et al. [74]), although they may play a role in the general case. Boundary conditions consisting of values for total pressure and temperature at the inflow, and time-varying static pressure for the outflow are obtained from experiments. Combustion is initiated by an energy deposition in computational cells falling within a sphere of radius 0.5 mm between the spark electrode and counter-electrode (Figure 3): 2.5 mJ for 0.5 CAD, to simulate the arc phase, and additional 2.5 mJ for 10 CAD, to simulate the glow phase, are released into the gas in agreement with the available measurement values [75].

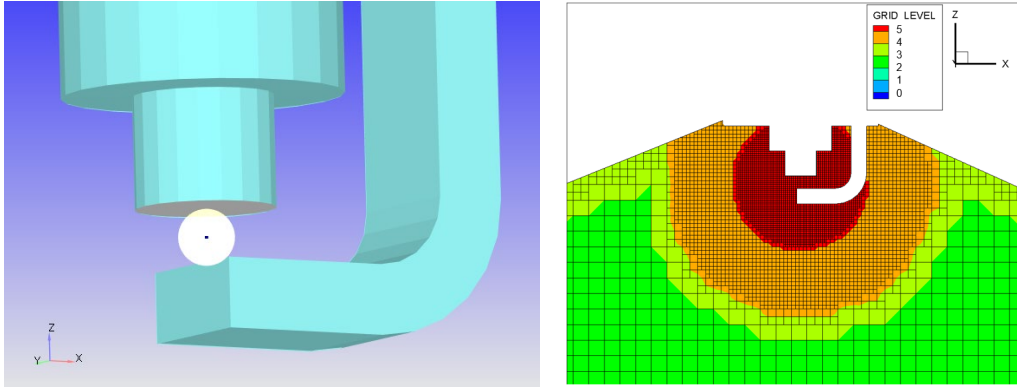


Figure 3. Ignition region views, with energy deposition sphere (left) and mesh resolution around the spark (right).

Various fixed mesh refinement and AMR strategies were used, ad-hoc temporally and spatially activated. Fixed refinement is used in the combustion chamber, around the throttle, in the valve seat regions and in the spark region. Velocity-based AMR is used to resolve flow structures in the cylinder and in the intake region; flame front during the combustion is resolved using AMR based on the thickening factor model variable. More details about the grid are provided in Table 2.

Table 2. Mesh details.

Maximum grid size in the combustion chamber	1 mm
Grid size in the valve region	0.5 mm
Velocity AMR size	1 mm
AMR size across the flame	0.25 mm
Minimum grid size, around the spark	0.125 mm

#### D. TFM COMBUSTION MODEL

TFM is based on the thermal flame theory and works by artificially thickening the laminar flame while preserving the laminar flame propagation speed  $s_l^0$ . A scaling transformation is applied to transported scalars [76, 77]. The species conservation equations, based on these scaling arguments, become

$$\frac{\partial \rho Y_i}{\partial t} + \frac{\partial \rho Y_i u_j}{\partial x_j} = \frac{\partial}{\partial x_j} \left( \rho \cdot E \cdot F \cdot D \frac{\partial Y_i}{\partial x_j} \right) + \frac{E}{F} \dot{\omega}_i \quad \text{Equation 1}$$

where  $\rho$  is the density,  $u$  is the velocity,  $Y_i$  are the species mass fractions, and  $\dot{\omega}_i$  the corresponding reaction rates. Multiplying the diffusivity  $D$  and dividing the reaction rate by the same thickening factor  $F$ , the flame is thickened to allow a proper resolution on the LES mesh, while maintaining the propagation speed. The efficiency function  $E$  accounts for the effects of unresolved SGS wrinkling. In Equation 1, the reaction rate term is multiplied by  $E/F$  and the mass diffusivity becomes  $E \cdot F \cdot D$ . Equivalent modifications are applied for the energy equation, where the same scaling is applied to the thermal and mass diffusivities. Local chemical kinetics is solved for the whole domain, not restricted to the flame region only.

The dynamic TFM formulation [78] allows to use an  $F$  value greater than 1 in the flame front, while  $F$  relaxes to 1.0 away from the flame front. In order to accurately resolve the flame front, laminar flame speed  $s_l^0$ , laminar flame thickness  $\delta_l^0$  and maximal fuel reaction rate  $|\dot{\omega}_i|_{1D}^{max}$  are tabulated from 1D laminar premixed flames computed at several equivalence ratios, pressures (in this case from 0.8 to 30 bar) and unburnt temperatures (in this case from 400 to 1400 K). The thickening procedure and a specific calibration analysis of TFM sub-models is reported in the following sub-sections.

### Flame sensor and thickening

In order to use the dynamic TFM formulation [78], it is necessary to know where the flame front is located, to avoid inappropriate thickening in non-reacting regions. The flame front is detected with a flame sensor  $S$  defined as

$$S = \max \left[ \min \left( \beta_S \frac{|\dot{\omega}_i|}{|\dot{\omega}_i|_{1D}^{max}} - 1, 1 \right), 0 \right] \quad \text{Equation 2}$$

where  $|\dot{\omega}_i|_{1D}^{max}$  is the tabulated maximal fuel reaction rate, which is a function of pressure, temperature, equivalence ratio and EGR, evaluated from off-line 1D steady laminar flame simulations.  $|\dot{\omega}_i|$  is the 3D chemical reaction rate at the location of interest calculated using a constant volume homogeneous reactor model and is affected by local conditions, and  $\beta_S$  is a model parameter controlling the sensitivity of the flame detection. This flame sensor  $S$  is adjusted according to the methodology of Jaravel [79], which enables to correctly locate the flame front in a detailed chemistry context, capturing the species gradients at the flame foot and tail. Iso-octane is used as the flame sensor species. An appropriate value of  $\beta_S$  is essential to detect the flame and for TFM to work correctly.  $S$  is equal to 1 in the reactive part of the flame front and drops to 0 outside this region, as shown in Figure 4.

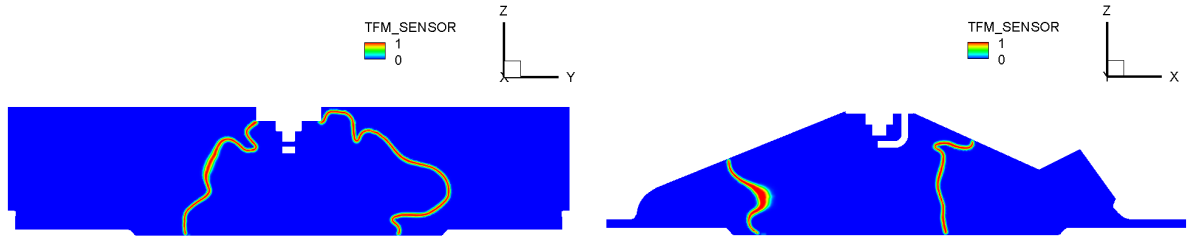


Figure 4. Flame sensor  $S$  at 5 CAD aTDC, on the YZ plane (left) and on the XZ plane (right).

The flame thickening factor  $F$  is calculated as

$$F = 1 + (F_{max} - 1)S \quad \text{Equation 3}$$

where the maximum value of the thickening factor in the flame is computed as:

$$F_{max} = \frac{n_{res} \Delta_x}{\delta_l^0} \quad \text{Equation 4}$$

$n_{res}$  is the user specified number of grid points across the flame,  $\Delta_x$  is the local grid spacing, and  $\delta_l^0$  is the tabulated laminar flame thickness. Thickening and efficiency procedures are disabled when the flame reaches the walls based on the distance to the wall.

### TFM start timing

The spark model used in this work is a simple energy deposition and does not attempt to model the complex phenomena underlying ignition. TFM combustion model is developed for premixed flames. In the first instants after the ignition, the kernel is not a propagating flame yet and the thickening procedure, that affects the ignition phase, may lead to quenching. To avoid this phenomenon, TFM is activated some crank angle degrees after ignition, or in other words, an appropriate activation timing is essential for TFM to work correctly. To better clarify this aspect a specific analysis is shown in Figure 5, where the maximum temperature (left) and the mass

fraction burned (right) at the time of ignition are reported. The green curve is obtained by activating the TFM at the same instant as the ignition timing (IT), while the red curve is obtained by activating the TFM 3 CAD after the ignition. The maximum temperature of the case where TFM is activated at IT is much lower because the thermal diffusivity is multiplied by  $E \cdot F$  due to the TFM, and the subsequent development of the combustion is significantly slowed down. This is expected since it is not ideal to thicken the flame when the flame kernel is not yet established and the thickening procedure is not applicable in the first stage of the kernel formation. The choice of the TFM activation timing is arbitrary and different values have been explored. In the current work, taking into account the time required for the flame kernel formation, the spark timing is set to -23 CAD aTDC and the TFM start timing is set to 3 CAD after the ignition which is -20 CAD aTDC. Further work will focus on a more systematic procedure to delay thickening activation.

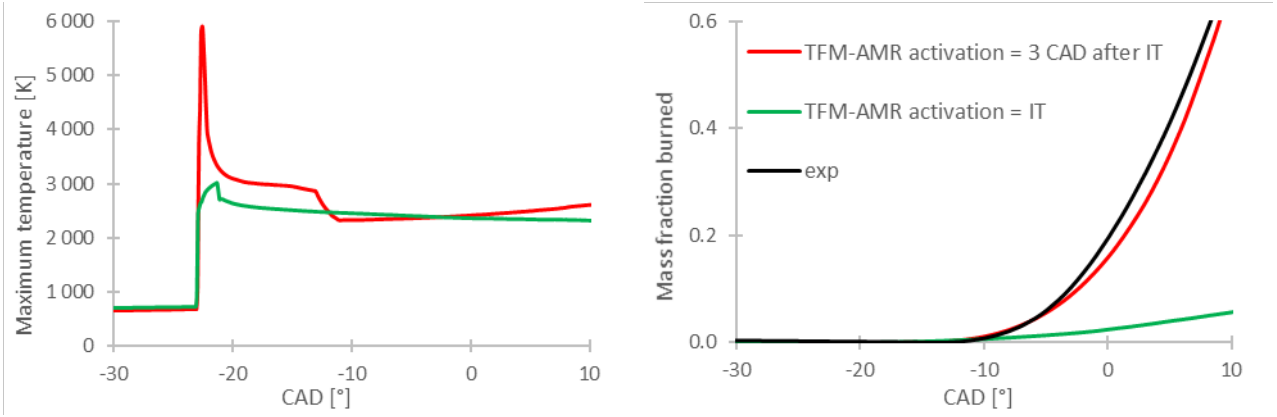


Figure 5. Maximum temperature (left) and mass fraction burned curves (right) at the time of the ignition and TFM start timing effect: TFM is activated at the same instant as the ignition (green curve) and 3 CAD after the ignition (red curve). The black curve is the experimental average cycle

## E. TFM-AMR COUPLING

In the dynamic TFM-AMR coupling context, the flame front is detected by the flame sensor  $S$  and AMR is thus activated when  $S > 0$  or, equivalently, when the flame thickening is active ( $F > 1$ ). In the present study, the AMR level  $n_{AMR}$ , is set so that the thickened flame thickness, given by  $\delta_F = n_{res} \Delta_x^{AMR}$ , is constant throughout the computation. Here,  $\Delta_x^{AMR}$  is the local flame resolution due the AMR, and the refinement level  $n_{AMR}$  is measured with respect to a base cell size  $\Delta_x^{base}$ . From the user defined parameter  $\delta_F$ , the AMR level is thus obtained as

$$n_{AMR} = \text{int} \left[ \frac{1}{\log(2)} \log \left( \frac{n_{res} \Delta_x^{base}}{\delta_F} \right) \right] \quad \text{Equation 5}$$

where  $\text{int}$  refers to the nearest integer function. Consequently, the AMR mesh size  $\Delta_x^{AMR}$  is calculated as

$$\Delta_x^{AMR} = \frac{\Delta_x^{base}}{2^{n_{AMR}}} \quad \text{Equation 6}$$

The thickening factor is finally given by

$$F_{target} = \frac{n_{res} \Delta_x^{AMR}}{\delta_l^0} \quad \text{Equation 7}$$

### Efficiency function

In order to take into account the effects of turbulence on the flame front, an efficiency function is introduced. The evaluation of this efficiency function is based on the model proposed by Charlette [61], and is calculated as the ratio between the total wrinkling of the flame and the wrinkling of the thickened flame, which is less sensitive to turbulent eddies:

$$E = \frac{\varepsilon|_{\Delta=\delta_l^0}}{\varepsilon|_{\Delta=F\delta_l^0}} \quad \text{Equation 8}$$

The wrinkling factor  $\varepsilon_\Delta$  is a function of the effective straining function  $\Gamma_\Delta$ , the laminar flame-speed  $s_l^0$ , the laminar flame thickness  $\delta_l^0$ , the subgrid-scale turbulent Reynolds number  $Re_\Delta$  and the subgrid-scale turbulent velocity  $u'_\Delta$  (Equation 9).

$$\varepsilon_\Delta = \left( 1 + \min \left[ \frac{\Delta}{\delta_l^0} - 1, \Gamma_\Delta \left( \frac{\Delta}{\delta_l^0}, \frac{u'_\Delta}{s_l^0}, Re_\Delta \right) \frac{u'_\Delta}{s_l^0} \right] \right)^\beta \quad \text{Equation 9}$$

Figure 6 shows the  $u'_\Delta$  (left) and the local heat release rate (right) field on a slice passing through the spark plug at 5 CAD aTDC. A drop is noticeable in the subgrid-scale turbulent velocity in the flame front due to the AMR, since  $u'_\Delta$  scales with  $(\Delta_x^{AMR})^2$ . This effect is due to the sudden change in resolution, since the SGS turbulence outside the flame is much larger. The turbulent field does not have time to fully decay in the flame front, as the AMR used to resolve the flame moves in the combustion chamber. Indeed, as the cells get finer, smaller turbulent scales are generated. The computation of  $u'_\Delta$  is however based on a fully developed turbulent energy cascade and does not take this effect into account, leading to an under-estimation of  $u'_\Delta$ .

To counteract this effect a very simple model is used, multiplying the subgrid-scale turbulent velocity by a factor  $\lambda$ , i.e., by replacing  $u'_\Delta$  with an effective value  $u'_{eff} = \lambda u'_\Delta$  in Equation 9. Figure 7 shows the effect of this turbulent velocity multiplier on the predicted mass fraction burned, using  $\lambda = 10$  (red curve) and  $\lambda = 15$  (green curve). The effect of this parameter is twofold. The first consequence is visible at the combustion beginning, with a faster start for a higher  $\lambda$  value. The second effect is observed in the main part of the combustion, where a faster combustion rate for a larger  $\lambda$  value is maintained until about CA90. This dependency of the subgrid-scale velocity fluctuation to the AMR level needs to be corrected, so that no ad-hoc scaling of  $u'_\Delta$  should be necessary.

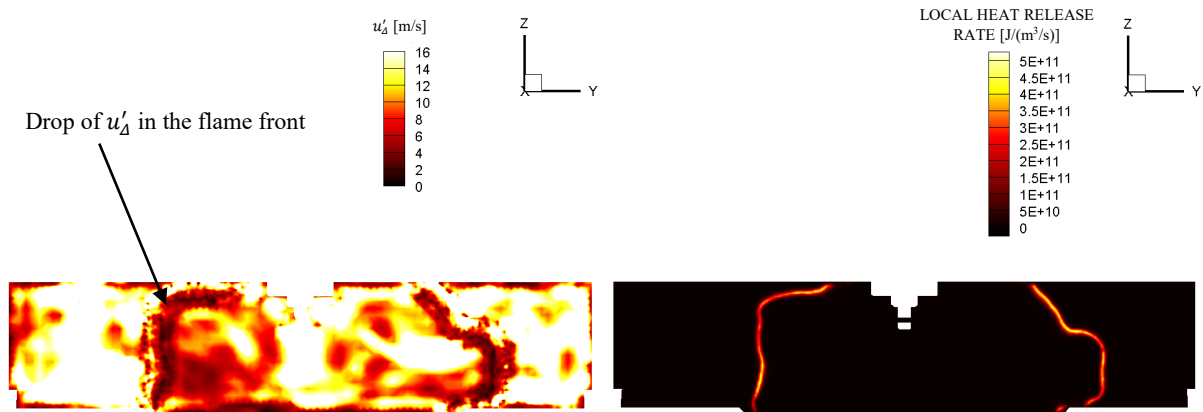


Figure 6. Subgrid-scale turbulent velocity (left) and local heat release rate (right) at 5 CAD aTDC on the YZ plane through the spark plug.

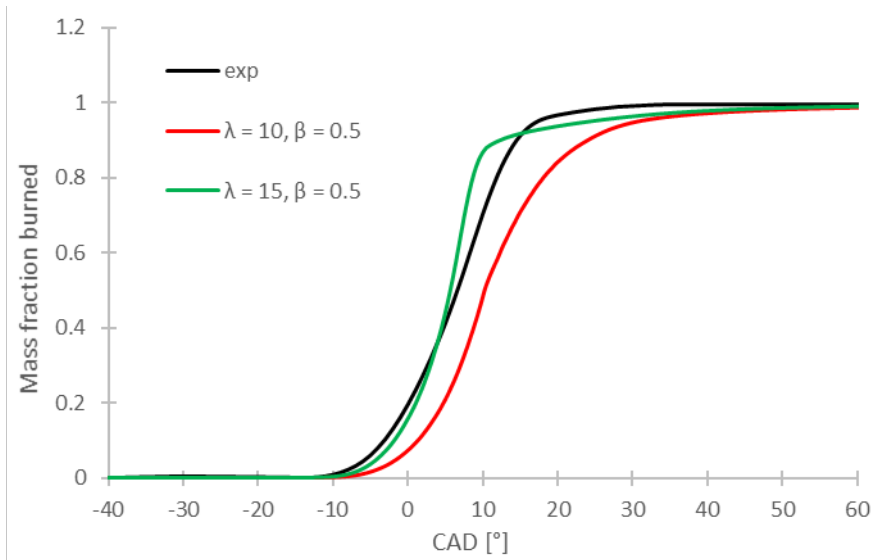


Figure 7. Effect of turbulent velocity multiplier,  $\lambda = 10$  (red curve) and 15 (green curve). The black curve is derived from the average of experimental engine cycles. Charlette's model  $\beta$  is set to 0.5 (Equation 9).

The wrinkling factor given by the Charlette's model formula (Equation 9) is also dependent on a second parameter, the exponent  $\beta$ , and this value also needs to be properly assessed. Figure 8 shows its effect, spanning  $\beta$  values of 0.5 (red curve), 0.6 (orange curve), 0.65 (green curve) and 0.8 (blue curve), with  $\lambda$  set to 10. It is worth noting that, in the current implementation,  $\beta$  is kept constant throughout the entire simulation, thus no dynamic adaptation is considered. The effect of this parameter on the combustion rate is similar to the effect of  $\lambda$ . Combustion is markedly faster as  $\beta$  value increases.

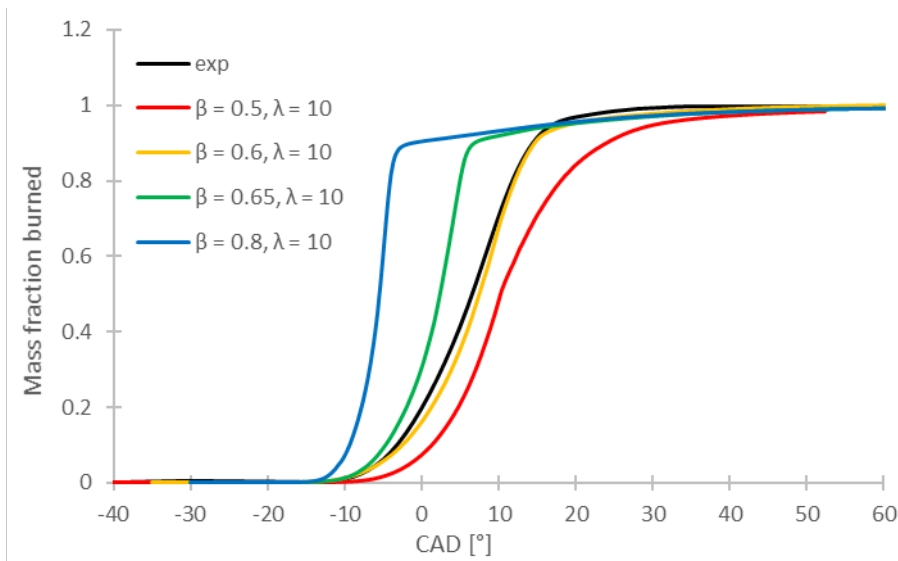


Figure 8. Effect of Charlette  $\beta$  value: 0.5 (red curve), 0.6 (orange curve), 0.65 (green curve) and 0.8 (blue curve). The black curve is the experimental average cycle.  $\lambda$  is set to 10.

### Grid sensitivity analysis

Grid resolution is of paramount importance in ensuring high quality of the LES results. A preliminary test is carried out to compare two different grid sizes to resolve the flame front. A high number of grid points across the flame front would be desirable to resolve the flame in the best possible way, but it would also lead to high computational costs. At the same time, using too few grid points in the flame front would not provide adequate and accurate results. For these tests, the number of grid points across the flame front,  $n_{res}$ , is set to 4 as a compromise between the accuracy of the results and the calculation time. Two different values of target flame thickness  $\delta_F$  (after thickening) are used. As shown in Table 3, if  $\delta_F = 1.0 \text{ mm}$  the corresponding resolution in the flame front is  $\Delta_x^{AMR} = 0.125 \text{ mm}$ , while a flame front resolution  $\Delta_x^{AMR} = 0.25 \text{ mm}$  is obtained if  $\delta_F = 1.5 \text{ mm}$ .

To assess the grid effect, Figure 9 shows the predicted mass fraction burned curves for a medium flame front resolution,  $\Delta_x^{AMR} = 0.25$  mm, and a fine resolution,  $\Delta_x^{AMR} = 0.125$  mm, with and without re-adaptation of the subgrid-scale turbulent velocity multiplier. The peak cell count varies substantially, from 1.5 M for the medium grid to 3.5 - 4.0 M for the fine grid cases, due to the AMR level obtained in the flame front. The combustion model is not fully mesh independent, if other parameters do not adapt. As visible, an under-estimation of the overall combustion progress is observed when a finer grid is applied, with the same  $\lambda$  value of 10. Of course, the turbulent velocity multiplier  $\lambda$  can be recalibrated to achieve the correct combustion speed, in this case setting it to  $\lambda = 14$ .

Views of the flame structure predictions are shown through contours of the temperature fields in Figure 10. Using a finer mesh on the flame, the resolved front is more wrinkled. The flame location is retarded if model parameters are not compensated, while the correct combustion progress is achieved for the optimal mesh-dependent  $\lambda$  choice. Table 3 summarizes the effect of thickened flame value  $\delta_F$  on the AMR level  $n_{AMR}$  and grid  $\Delta_x^{AMR}$ .

Table 3. AMR level and grid calculations.

$n_{res}$	$\Delta_x^{base}$	$\delta_F$	$n_{AMR}$ (Eq. 7)	$\Delta_x^{AMR}$ (Eq. 8)	$\lambda$ (Eq. 10)	$\beta$ (Eq. 10)	Peak cell count
4	8 mm	1.5 mm	5	0.25 mm	10	0.6	1.5 M
4	8 mm	1.0 mm	6	0.125 mm	10	0.6	3.5 M
4	8 mm	1.0 mm	6	0.125 mm	14	0.6	4.0 M

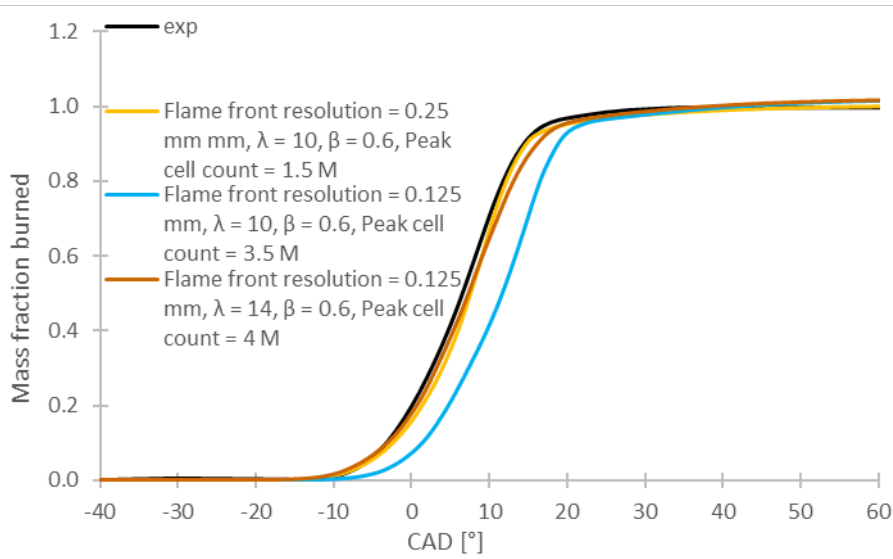


Figure 9. Grid sensitivity analysis, with a flame front resolution  $\Delta_x^{AMR} = 0.25$  mm and optimal  $\lambda = 10$  (orange),  $\Delta_x^{AMR} = 0.125$  mm and  $\lambda = 10$  (cyan) and  $\Delta_x^{AMR} = 0.125$  mm and optimal  $\lambda = 14$  (brown). The black curve is the experimental average cycle.

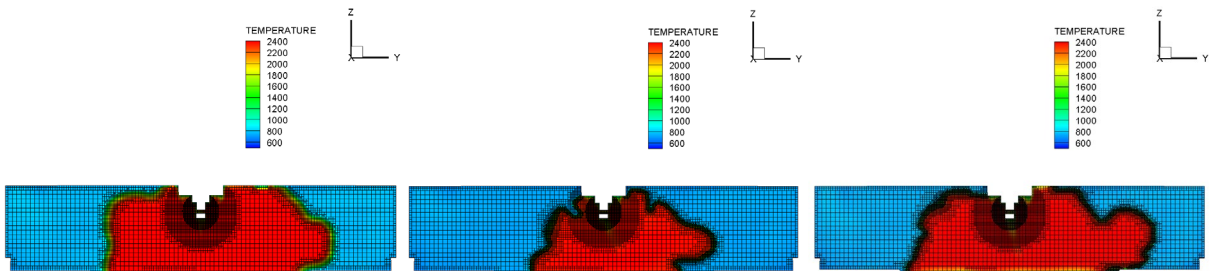


Figure 10. Temperature field at 5 CAD aTDC, on the YZ plane, with a flame front resolution  $\Delta_x^{AMR} = 0.25$  mm and optimal  $\lambda = 10$  (left),  $\Delta_x^{AMR} = 0.125$  mm and  $\lambda = 10$  (middle) and  $\Delta_x^{AMR} = 0.125$  mm and optimal  $\lambda = 14$

Based on the overall parameter and grid explorations presented above, the subsequent results presented in this work use a thickened flame value,  $\delta_F$ , set to 1.5 mm, with a corresponding flame front resolution  $\Delta_x^{AMR} = 0.25$  mm, to guarantee a reasonable and affordable calculation time, in the order of 3 days per cycle on 120

cores. The corresponding optimal setting of the model parameters is as follows: turbulent velocity multiplier  $\lambda = 10$  and Charlette's wrinkling model exponent  $\beta = 0.6$ . An additional research effort is needed in the future in order to improve the predictivity of the proposed approach as it is based on various modeling parameters for which the generalization is not guaranteed at this stage of model development.

## F. RESULTS AND DISCUSSION

### *Assessment and validation of the LES results*

We begin the engine results analysis by evaluating the numerical model's capability to reproduce the experimental cycle-to-cycle variations. The results of 20 consecutive LES cycles are compared against the corresponding measured quantities acquired on the optical engine at stoichiometric conditions. Because the optical engine has non-negligible blow-by, and the mass loss through the rings-liner gap is not modeled, the simulated and measured pressure traces are not directly comparable. For this reason, the comparison is made using non-dimensional quantities, such as the mass fraction of burned gases, combustion phasing, normalized pressure and flame imaging.

Figure 11 compares the mass fraction burned curves,  $x_b$ , calculated from the 20 LES cycles (right) with the experimental data obtained from 100 engine cycles (left). Black curves on the left are the experimental cycles, while grey curves on the right are the simulated cycles. Simulation results accurately reproduce the cyclic variability observed in the experiments, as the curve bundle width is very similar, and combustion rates are satisfactorily predicted. However, the comparison between experimental and numerical average cycles (Figure 12) suggests that combustions predicted by the LES are slightly slower than the experimentally observed cycles. At the same time, the coefficient of variation of the indicated mean effective pressure (COV of IMEP) is well reproduced, since a value of 1.3% is obtained from the simulations and a value of 1% is measured in the experiments.

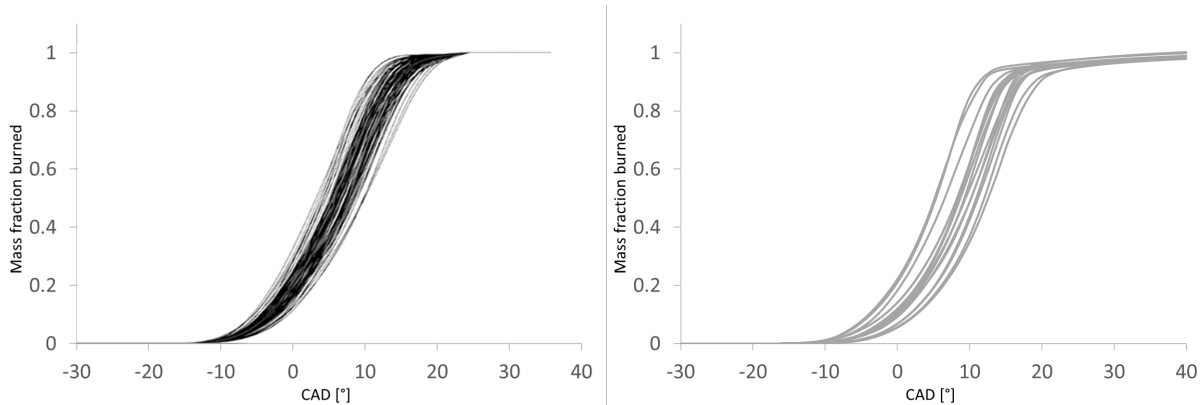


*Figure 11. Comparison of mass fraction burned curves: 100 experimental cycles (left) and 20 LES cycles (right).*

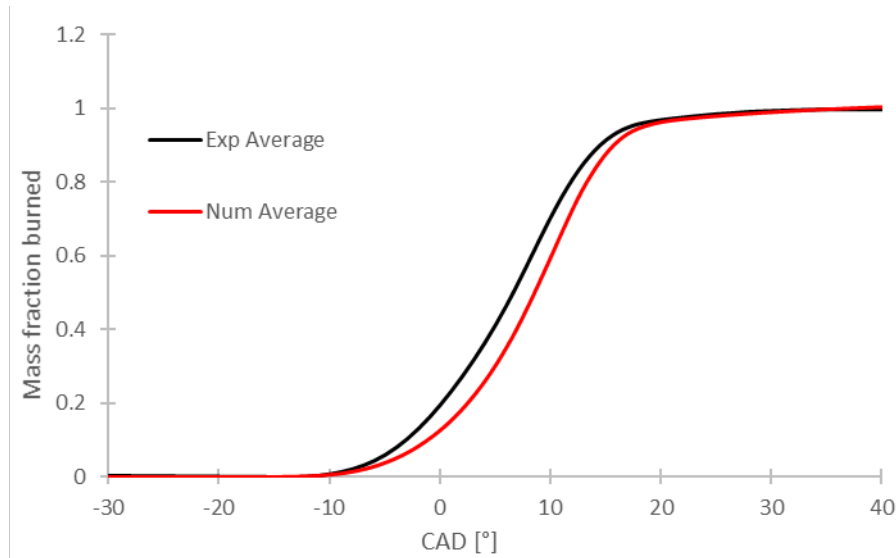


Figure 12: Comparison of mass fraction burned curves between experimental average cycle (black) and numerical average cycle (red).

Figure 13 presents a Matekunas diagram [80], built plotting normalized peak pressures of each cycle against the crank angle of their occurrence. Normalized values are used for the unaccounted blow-by reason previously mentioned. Peak pressures are normalized by dividing the actual values by the average value of the corresponding experimental or numerical dataset. Both measured and computed data are mainly scattered around a straight line, indicating a stable combustion regime, as suggested by Matekunas.

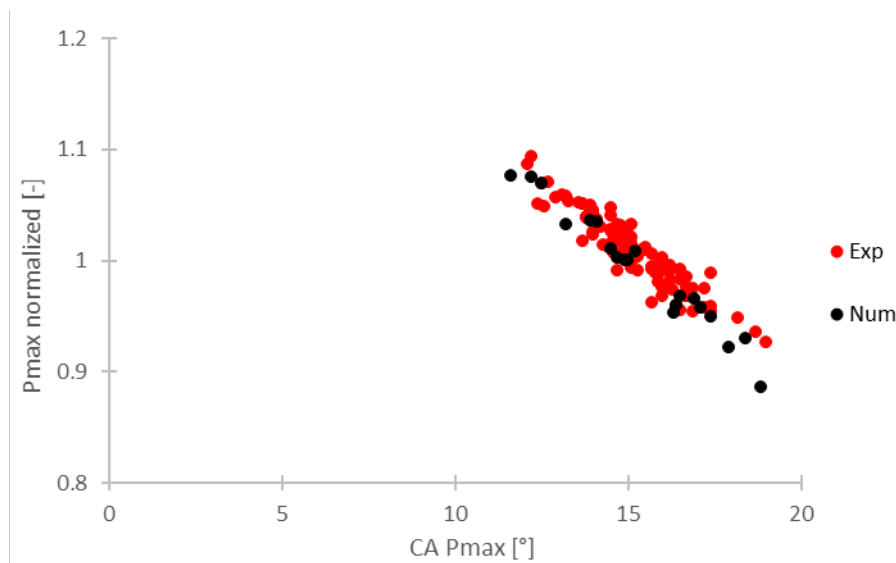


Figure 13. Matekunas diagram: comparison between experimental (red) and numerical (black) combustion events.

In order to perform a more quantitative assessment of the LES capability in reproducing the experimental CCV, Figure 14 provides an analysis of typical combustion metrics. The CA5 (blue), CA50 (red) and CA90 (green) values are defined as the crank angles after the ignition timing at which the burned gases mass fraction reaches 5%, 50% and 90%, respectively. Vertical lines represent average values, while solid symbols represent individual cycles. The CA5 is representative of the ignition phasing, while CA50 and CA90 correspond to the turbulent flame propagation. The results show that the LES model satisfactorily reproduces the experimental behavior, although it predicts slightly delayed CA5 and CA50 compared to the measured values, by about 3 CAD. As a matter of fact, the predicted coefficient of variation of the CA5, CA50 and CA90 are quite close to the experimental values, and the maximum discrepancy is less than 0.32%, thus confirming that the cycle-to-cycle variability is well reproduced.

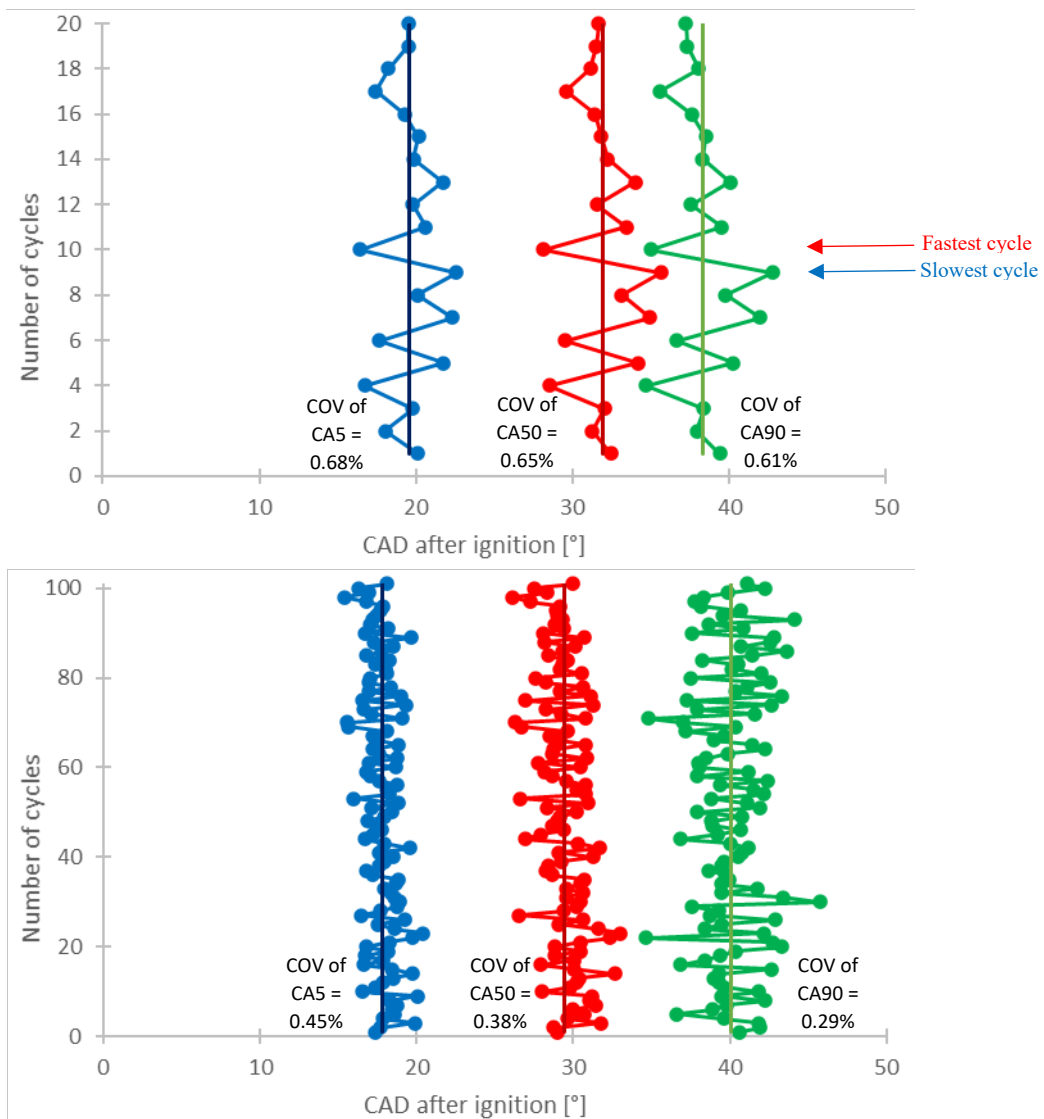


Figure 14. Combustion phasing for 20 LES cycles (top) and 100 experimental cycles (bottom): CA5 (blue), CA50 (red), CA90 (green).

In addition to overall combustion and indicated quantities, a more detailed validation can be based on the analysis of the flame structure. Figure 15 shows sequences of flame propagation images, comparing experiments and LES results. The simulated fastest cycle, n. 10, and slowest cycle, n. 9, based on the mass fraction burned curves, are selected and displayed against fast, medium and slow experimental cycles. The comparison provides a visualization of the flame structure. Red circles mark the outlines of the optical access. Numerical images are obtained with a volume rendering of the temperature field in the range 1200-2200 K. Experimental images represent the natural flame luminosity captured by the high-speed camera. Six different timings are reported. From this qualitative comparison, it can be seen how the experimental flames first start from a small kernel after spark time and then develop into a turbulent flame front at about -8 CAD aTDC. The flame kernel of the fastest numerical cycle propagates quickly in the chamber, even faster than in the experiments, while for the slowest numerical cycle the flame is able to propagate outside the spark electrodes starting from -12 CAD aTDC in agreement with the experimental images. From -8 CAD aTDC, the experimental flame starts to exhibit clear combustion asymmetry, since the flame is stretched and slightly convected towards the exhaust valves as a result of residual bulk charge motion. A similar behavior is reproduced in the model, for which the flame is however more centrally spread. From -4 CAD aTDC, the flame expands more along the direction of the chamber roof edge, as expected due to the larger volume available, and this effect is coherently seen in the simulations. The flame growth of the simulated cycles is slightly overestimated compared to the experiments. The flame reaches the optical access limit at about -4 CAD aTDC for the simulated fastest cycle and 8 CAD later for the slowest one, i.e. at 4 CAD aTDC. Lastly, at 12 CAD aTDC medium and fast experimental flames have exceeded the limit of optical access. At the same time, the numerical fastest flame has reached the liner while the slowest one is still away from the cylinder liner and its slow part is crossing the optical limit similarly to the experiments, on the intake side.

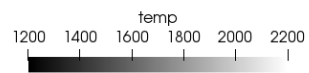
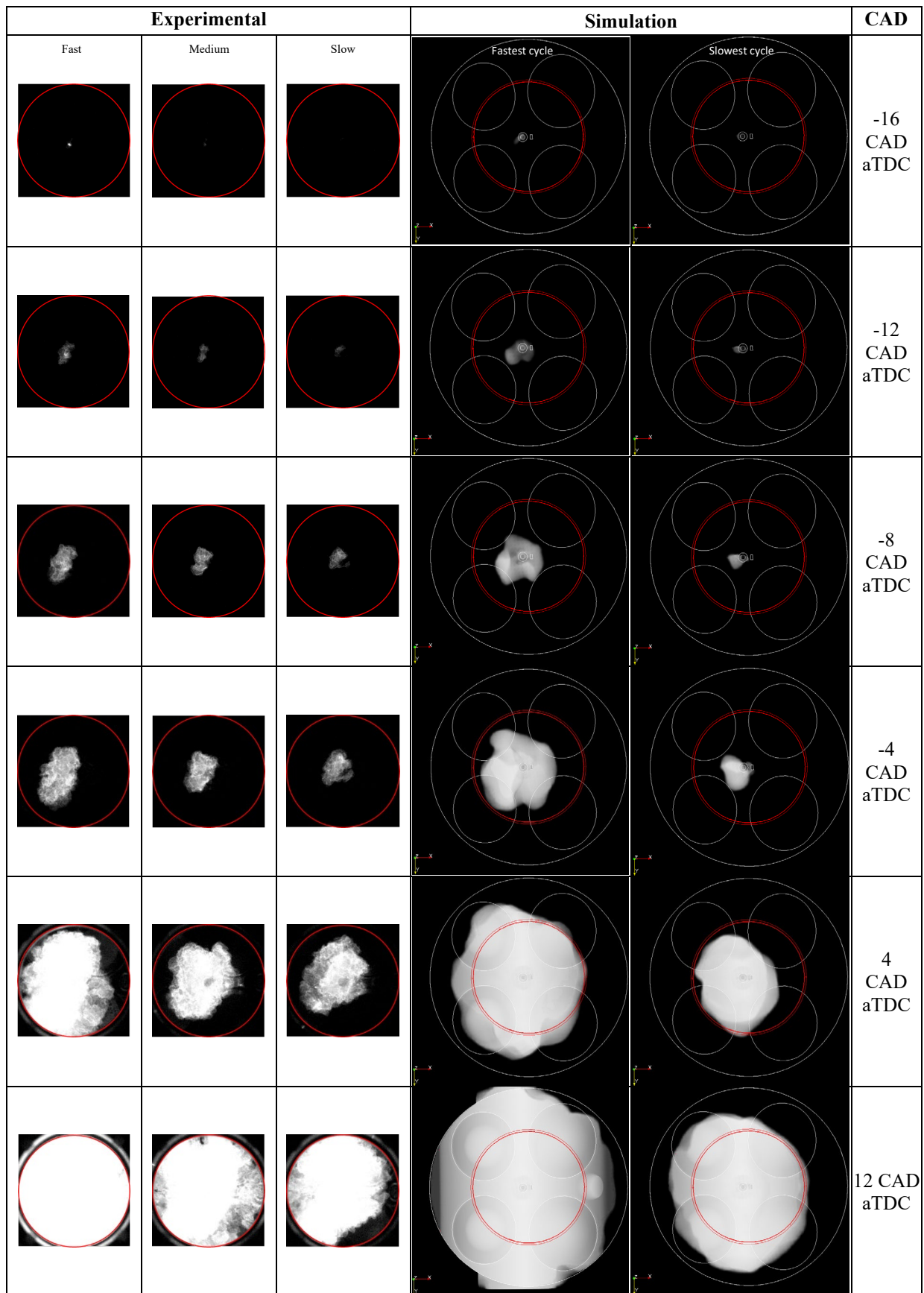


Figure 15. Qualitative comparison of measured and numerical flame propagation.

Overall, the comparison is reasonable in many aspects, however the macroscopic shape and details of the flame would certainly improve using a more refined grid. The results highlight that the global parameters characterizing the cyclic variability are well reproduced. A thorough investigation can be conducted on this dataset, analyzing local variables, in order to identify and describe the main sources of CCV. This detailed analysis is presented in the next section.

### *Analysis of the slowest and fastest cycle*

By comparing the slowest and fastest cycle obtained by the LES, we aim to identify the major contributors to the variations observed in the early flame kernel. The model assumes a premixed air-fuel composition and in the literature a consensus is found regarding the small impact of species turbulent fluctuations in PFI engines [53, 60], therefore the only factors that are probed are the turbulent fluctuations of the thermal and velocity fields. Figure 16 shows the simulated flame propagation around the spark location, for the slow and fast LES cycles, at five instants after the spark on two perpendicular cut planes passing through the spark plug. Differences in the flame propagation over time reflect differences in the overall combustion behavior. In particular, the flame shape strongly varies in terms of local wrinkling and surface area. The slowest cycle shows a little flame kernel, whereas the fastest cycle is characterized by a larger burnt gas zone and a wider flame surface. The flame expansion highlights that for the slowest cycle the flame kernel hardly propagates out of the spark plug gap, and it is mainly confined between the electrodes. On the other hand, the fastest cycle flame is able to propagate outside the spark plug gap from the very beginning, and grows much faster inside the chamber.

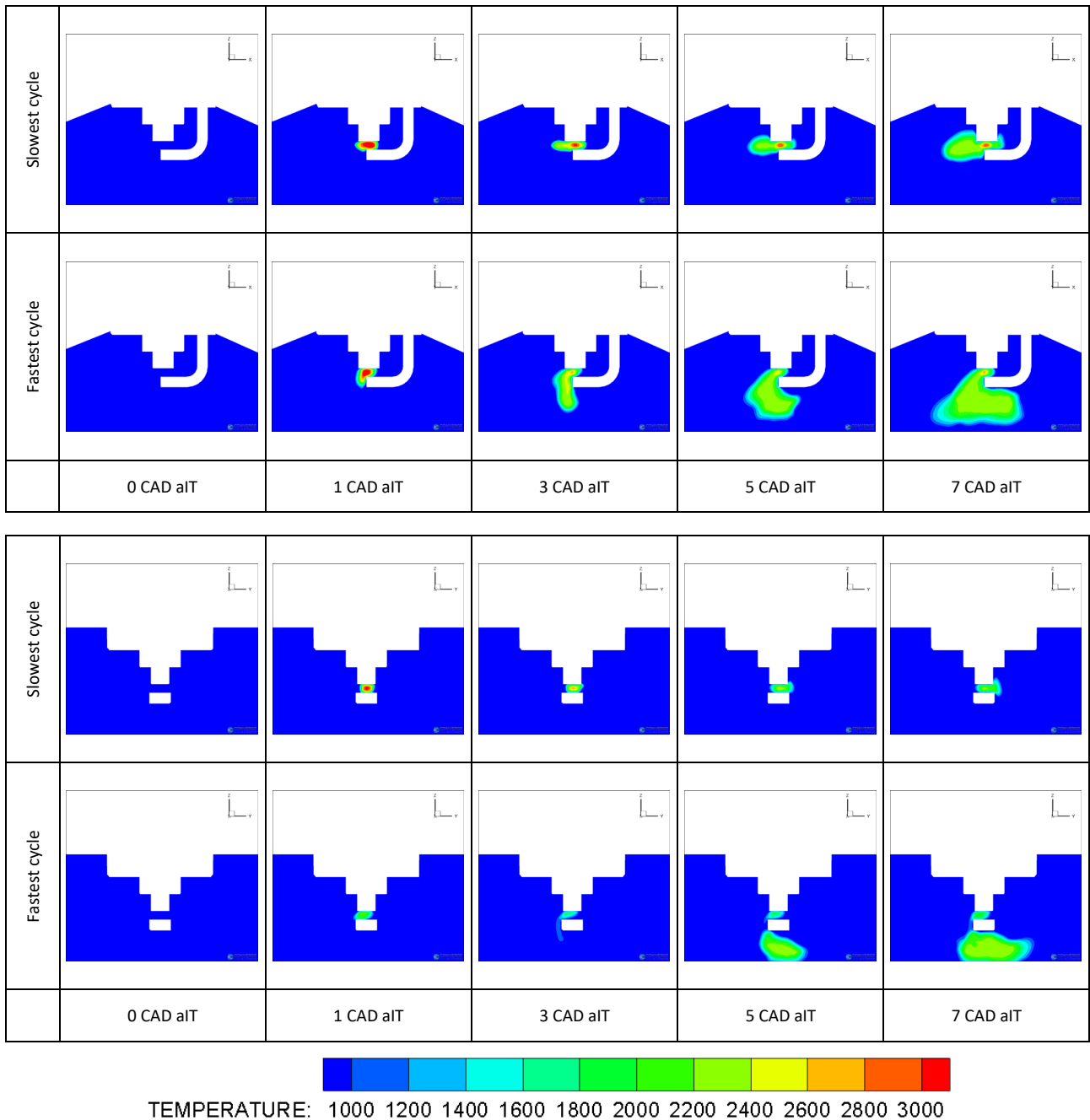


Figure 16. Temperature fields (range 1000-3000 K), for the fastest and slowest cycle at 0, 1, 3, 5 and 7 CAD after ignition timing. XZ plane (top), YZ plane (bottom).

Analyzing the corresponding instantaneous velocity fields resolved by the LES, we observe significant differences between the fastest and slowest combustion. Figure 17 shows a comparison of the simulated velocity magnitude around the spark location, in the range 0 to 5 m/s. In the slowest cycle the velocity magnitude observed between the electrodes is about 2 m/s, while the fastest cycle has a velocity of about 5 m/s. This aspect is likely one of the reasons for creating a faster flame development and increased wrinkling, but, distinguishing between the effects of the average values and of the fluctuations requires more analyses, which will be addressed in the following.

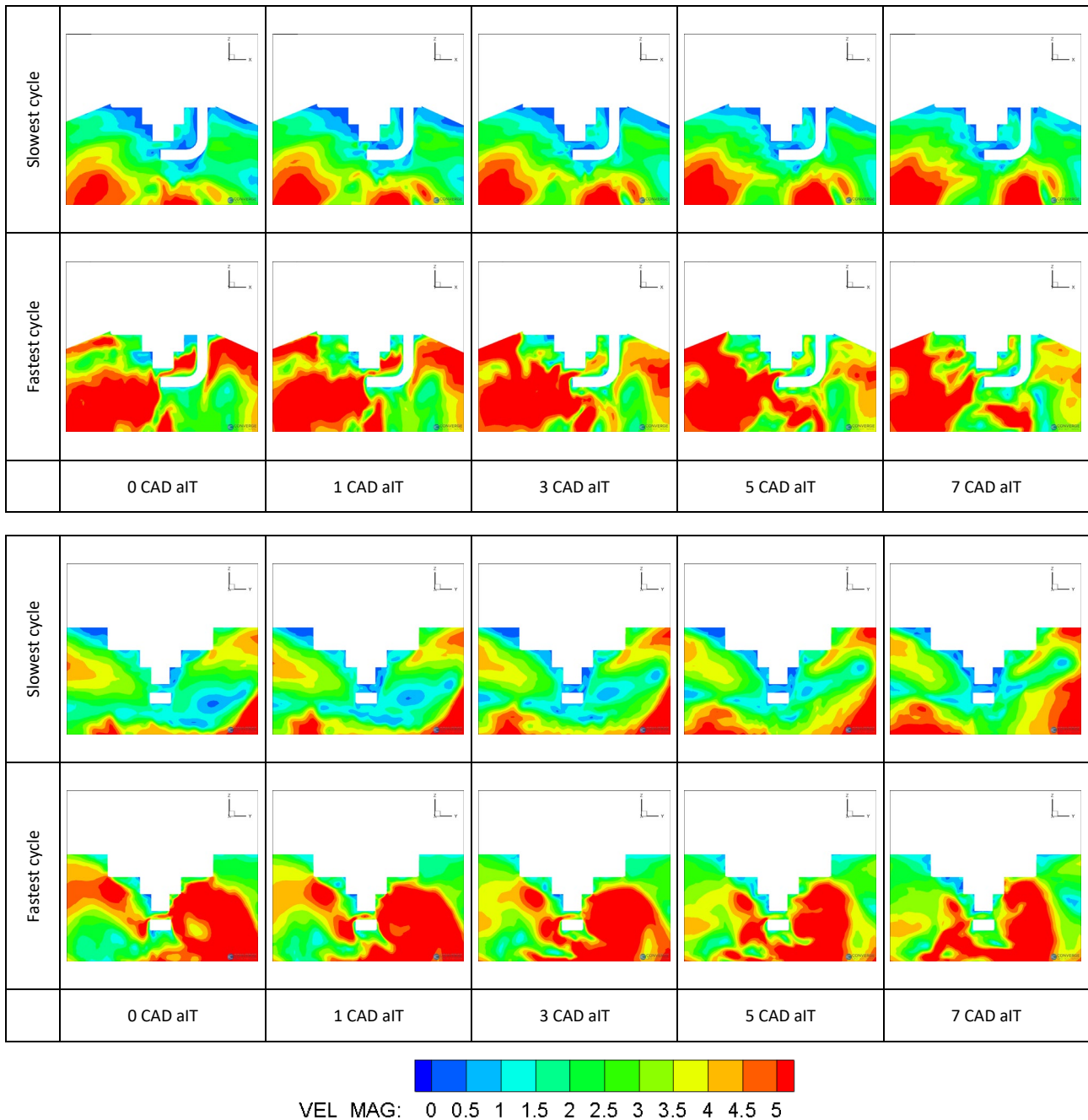


Figure 17. Velocity fields (range: 0m/s-5m/s), in the fastest and slowest cycles at 0, 1, 3, 5 and 7 CAD after ignition timing. XZ plane (top), YZ plane (bottom).

To better evaluate the interaction between the flow field and the flame development, Figure 18 shows a quantitative analysis of the probability density distributions of the velocity magnitude and temperature inside the flame front, 3 CAD (top) and 5 CAD (bottom) after ignition, with bin sizes of 0.2 m/s and 50 K, respectively. The velocity field just before spark timing will be analyzed and discussed in more details later. In red is the fastest cycle, and in blue the slowest. This distribution is obtained by solely considering the cells within the flame with a flame sensor value  $S > 0.1$  (Equation 2); thereby PDFs represent the distribution of the resolved velocity magnitude and resolved temperature, within the flame front. The flame front of the fastest cycle is characterized by a much wider range of velocity values, as opposed to the slowest cycle. In particular, the flame front in the fastest cycle is subject to large velocity levels reaching 10 m/s, while the slowest cycle is limited to about 3 m/s at most. Turbulence is therefore much higher in the fast burning flame. The analysis of these two velocity PDFs confirms that the differences between the fastest and the slowest cycle, previously observed through images around the spark region, are already present during the first instants of the flame kernel development. This behavior is consistently visible both at 3 CAD and 5 CAD after the spark timing. The turbulent intensity averaged in the flame zone is about 30% in all cases, but both the mean velocity and

turbulent velocity are much larger for the fast cycle (mean  $\sim 5.5$  m/s and fluctuation  $\sim 1.7$  m/s) than for the slow cycle (mean  $\sim 1.9$  m/s and fluctuating  $\sim 0.7$  m/s). The temperatures PDFs, on the contrary, have a much narrower distribution with respect to their mean values. In particular, the turbulence temperature fluctuation intensity on the flame does not exceed 20%, and more importantly mean and fluctuating components do not change much from the slow burning to the fast burning case.

In essence, from these results, it is apparent that the overall combustion is strongly correlated to both the mean and fluctuating components of velocity field on the flame, while the temperature field denotes a very mild correlation. In other words, these results suggest that the velocity field plays a critical role in the initial kernel development, and it is likely the dominant factor for the observed cyclic variability.

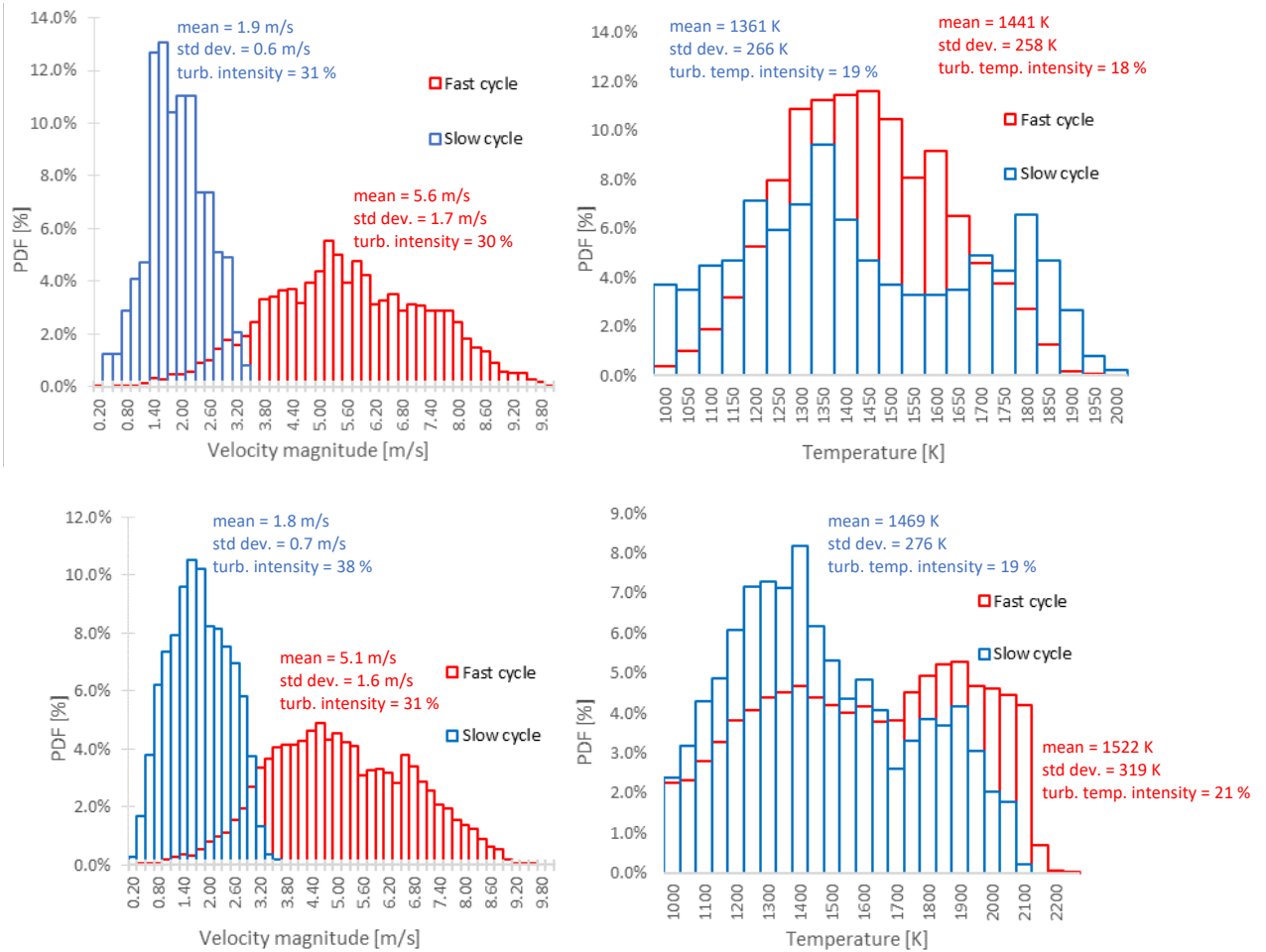


Figure 18. Probability density function of the resolved velocity magnitude and temperature, in the flame front, 3 CAD (top) and 5 CAD (bottom) after ignition.

Similar conclusions can be obtained from another point of view, still analyzing the flame front region. Figure 19-left shows the mean total fuel reaction rate, for the two cycles, which is defined as

$$\langle \dot{\omega}_{f,tot} \rangle = \int_F^E \dot{\omega}_f dV \quad \text{Equation 10}$$

while Figure 19-right shows the mean resolved fuel reaction rate, defined as

$$\langle \dot{\omega}_{f,res} \rangle = \int_F^1 \dot{\omega}_f dV \quad \text{Equation 11}$$

Figure 20 shows the mean efficiency function traces, defined as the ratio between the mean total and the mean resolved fuel reaction rate

$$\langle E \rangle = \frac{\langle \dot{\omega}_{f,tot} \rangle}{\langle \dot{\omega}_{f,res} \rangle} = \frac{\int_F^E \dot{\omega}_f dV}{\int_F^1 \dot{\omega}_f dV} \quad \text{Equation 12}$$

The comparison between the mean total and the mean resolved fuel reaction rate indicates that, with the current mesh resolution, about 20% of fuel reaction rate is resolved, while the remaining 80% is modeled. Moreover, the mean resolved fuel reaction rate is proportional to the flame surface. This confirms that the flame surface for the fastest cycle grows more quickly than the flame of the slowest cycle, and the combustion process is faster both during the ignition phase and during the turbulent combustion development.

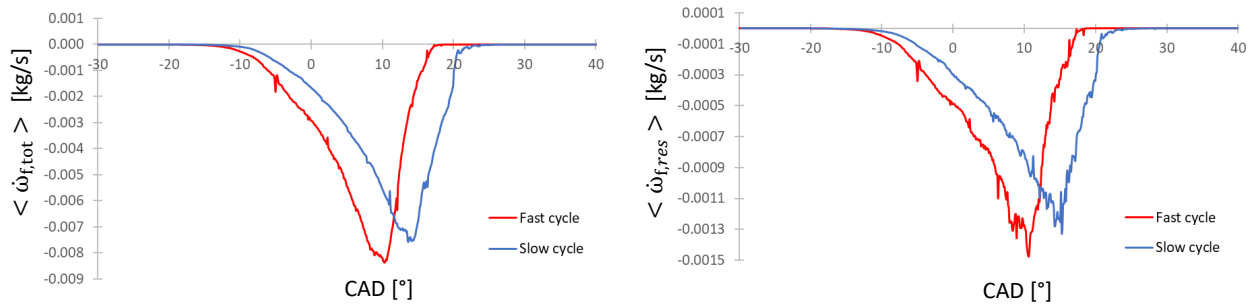


Figure 19. Comparison of mean total (left) and resolved (right) fuel reaction rate.

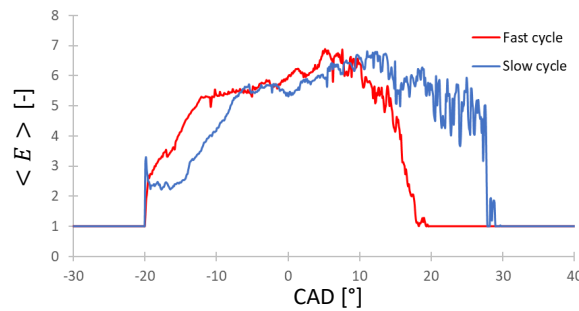


Figure 20. Comparison of mean efficiency function.

By extending the analysis of the turbulent fields to the time instants preceding the spark, we can investigate the correlation between pre- and post-ignition. Figure 21 shows a quantitative analysis of the probability density functions of the velocity magnitude and temperature in a sphere around the spark (with radius of 0.004 m), 5 CAD before the spark. These graphs show that the large velocity differences between the fast and the slow cycle previously observed in Figure 18 are already present before the spark. The PDFs of the resolved velocity magnitudes in the spark region before the spark activation show significant differences between slow and fast cycles. Velocity levels are also very similar to what is observed in the flame front, with maximum values around 9.0 m/s in the fastest cycle and only 4.2 m/s in the slowest cycle. Mean and fluctuating velocities are also quite similar to the flame front data. Conversely, the temperature field before the spark timing exhibits very small variations that are not transported to the combustion behavior, so becoming negligible on the flame. Mean temperature is actually higher for the slow burning case, supporting the idea that temperature does not affect the behavior of the overall combustion process.

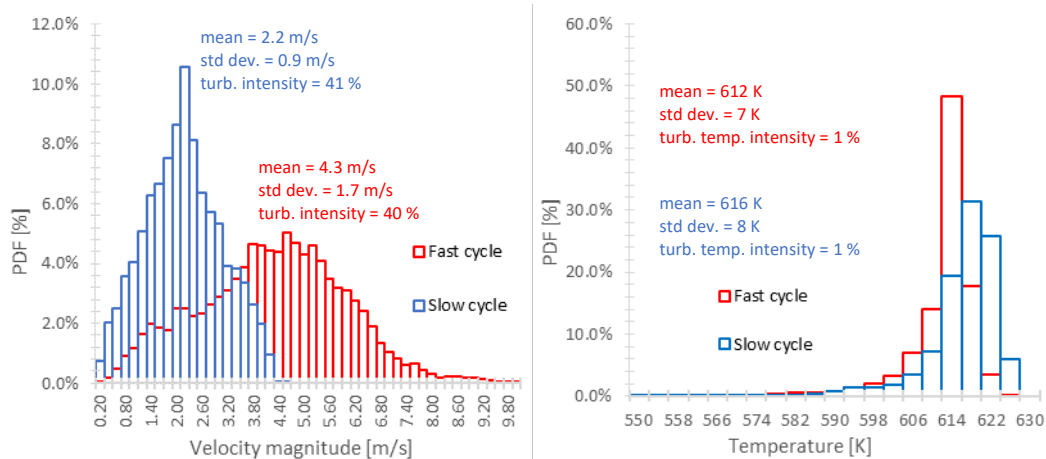


Figure 21. Probability density function of the resolved velocity magnitude and temperature in a sphere around the spark location, 5 CAD before ignition.

To provide additional insights on temporal correlations, Figure 22 shows the time history of the velocity magnitude monitored between the spark electrodes. The fast burning cycle is characterized by a velocity magnitude in the spark region constantly larger than the slow cycle, both before and after the ignition (occurring at -23 CAD aTDC). This velocity differential between the two cycles is maintained for the entire combustion process. Figure 23 shows a scatter plot of combustion phasing for the 20 LES cycles (CA1 in orange, CA5 in blue, CA50 in red and CA90 in green) as a function of time-averaged and fluctuating velocity at a monitor point between the spark electrodes, prior to ignition (from -40 CAD to -24 CAD). This analysis reveals that there is a correlation between the velocity field before ignition and the consequent turbulent flame propagation speed. In particular, cycles characterized by a fast combustion rate are those which have high values of both mean and fluctuating velocity between spark electrodes before the ignition, while, on the contrary, cycles characterized by a slow combustion rate are those which have a low velocity between spark electrodes before the ignition. This phenomenon is linearly and monotonically distributed across all numerical cycles in the range between the fastest (cycle n.10) and slowest (cycle n.9) cycles. Interestingly, and as opposed to the flame spatial averages, by performing time-averages of point velocity data, turbulence intensity correlates with combustion speed, as we move from the fast to the slow cycles. Therefore, it can be concluded that not only the velocity amplitude matters, but also the relative strength of the turbulent component.

The overall analysis leads also to the conclusion that from the velocity field before the spark, it is possible to infer the velocity field of the initial kernel development, before the turbulent combustion regime begins. Therefore, also the CCV correlates with the velocity field in the spark region before the ignition.

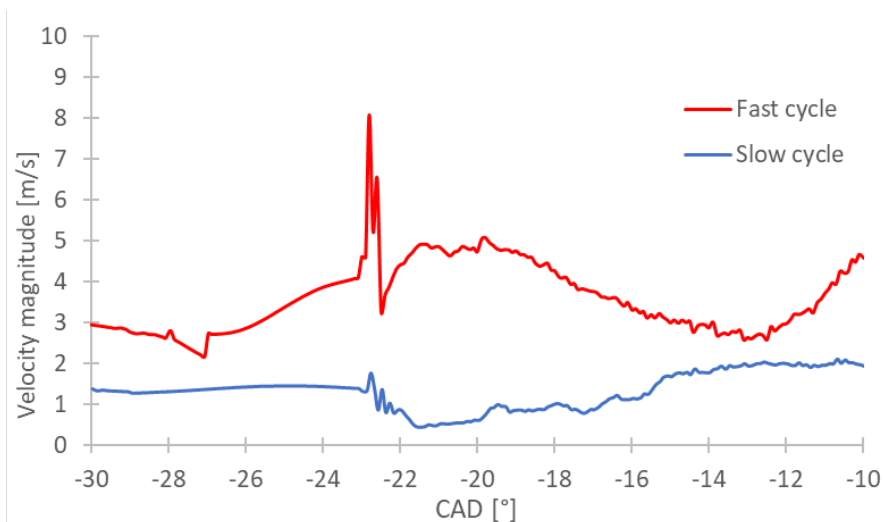


Figure 22. Resolved velocity magnitudes in a monitor point between spark electrodes.

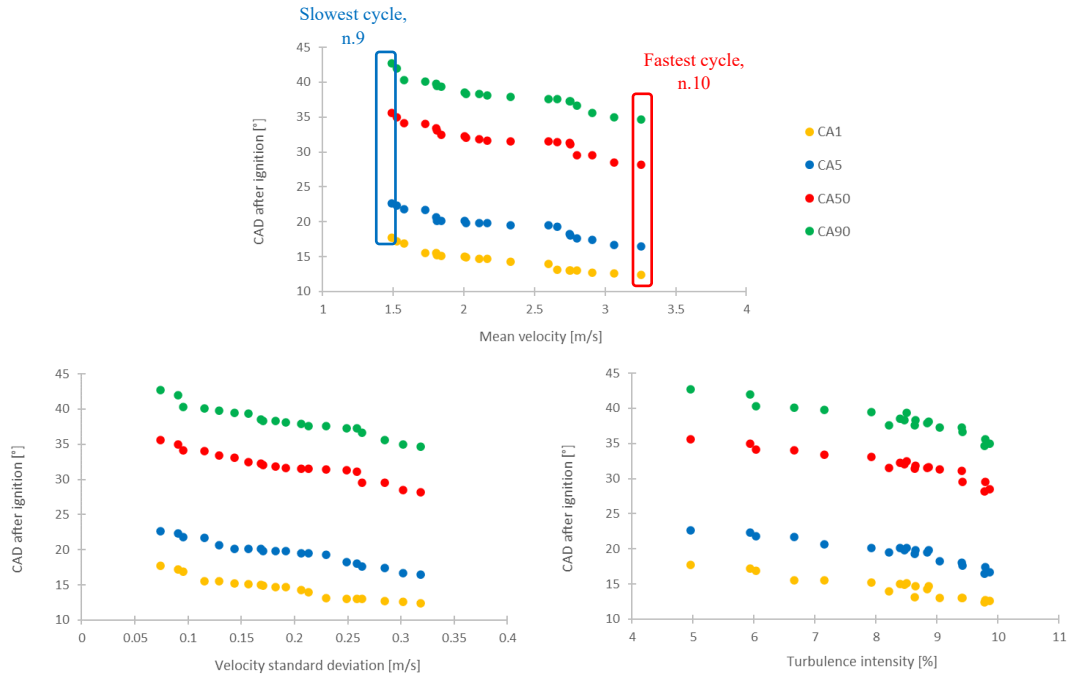


Figure 23. Scatter plot of combustion phasing for 20 LES cycles as a function of mean velocity magnitude (mean, fluctuation and turbulence intensity) at a monitor point between spark electrodes, averaged from -40 to -24 CAD (prior spark timing).

## G. CONCLUSIONS

This paper presents comparisons between large-eddy simulations and experimental measurements in a SI optical access engine, using TFM-AMR combustion model, in order to provide insights into the CCV origin. This is an early attempt to use the thickened flame model coupled with adaptive mesh refinement on the flame for engine LES simulations. After a preliminary investigation on the main model parameters (flame front detection algorithm, flame resolution, total flame wrinkling, and model activation timing), an appropriate setting has been defined for the engine case under investigation. The main findings related to the investigation of the cycle-to-cycle variation are listed below:

1. 20 LES cycles results were compared with 100 experimental cycles in terms of burned gas mass fraction, Matekunas diagram, combustion phases, flame images, and COV of IMEP. CFD results agree reasonably well with the experiments, especially looking at combustion global parameters. Simulations accurately reproduce the cyclic variability observed in the experiments, and combustion rates are satisfactorily predicted. The comparison between experimental and numerical average cycles suggests that combustions predicted by the LES are slightly slower than the experimentally observed cycles. However, the COV of IMEP is well reproduced, as a value of 1.3% is obtained from the simulations vs. a value of 1% from the experiments. Also, the maximum discrepancy between the predicted COV of CA5, CA50 and CA90 is less than 0.32% compared to experimental values, thus supporting that the cycle-to-cycle variability is well reproduced by the simulations. The Matekunas diagram analysis indicates that the investigated engine point represents a stable combustion condition, since both the measured and calculated data are mainly scattered on a straight line.
2. Detailed investigations and comparisons of the fastest and slowest cycles revealed a correlation between the local velocities and CCV. Local flow fields around the spark plug and around the spark timing were investigated through flame images and analysis of the probability density function of resolved velocity. Results highlight that the resolved velocity field plays a critical role in the growth of the early flame kernel, and it is the main factor determining the speed of the flame kernel growth of each specific cycle, thereby controlling the CCV. This conclusion remains probably true for most spark ignited premixed charge combustion engines at low IMEP. Temperature fluctuations, on the contrary, revealed to be quite insignificant.
3. Correlations between the velocity magnitude and turbulence intensity before and after the spark have shown that it is possible to predict the cyclic variability based on the local velocity data. Information

obtained from the analysis of the velocity field around the spark region is a valuable indicator of the rate of the combustion process.

Last but not least, this study shows that LES simulations with coupled TFM-AMR combustion model are a viable and promising approach, which however might need further developments and validations to be used as a predictive model in the LES of internal combustion engines. Areas for further improvements and analyses are identified, and listed below.

From the model development point of view, the coupled TFM-AMR robustness can be improved:

- Currently, ignition is not specifically modeled. A specific ignition sub-model to manage the transition from the initial kernel towards the flame regime is needed.
- The standard TFM wrinkling models are not directly transferrable to cases with adaptive mesh refinement on the flame, because of the error induced by AMR on the estimation of the velocity fluctuation. Further developments might consider a dynamic model for the SGS wrinkling, as anticipated in [81, 82], to self-adapt locally over the entire combustion process, up to the flame-wall interaction. An alternative route, which is today under investigation, is to propose a reliable model for the velocity fluctuation, even when AMR is used.

To extend the validation and the CCV analysis and prediction capability to different engine operating conditions, simulations of lean engine points are planned. In addition, non-premixed SI conditions shall be investigated to assess the contribution of the mixture composition fluctuations on the cycle-to-cycle variability.

## ACKNOWLEDGEMENT

The computational resources provided by the Italian Cineca consortium under the Iskra initiative - awards openPG19 and SimRFmix HP10CEH3NA, 2019-2020 - on the supercomputer Marconi are acknowledged. The student mobility support received by Dr. Jacopo Zempi through the Erasmus Traineeship program is also acknowledged. The work was partially performed at Convergent Science GmbH, Linz, Austria, during his exchange program.

## CREDIT AUTHORSHIP CONTRIBUTION STATEMENT

**Jacopo Zempi:** Conceptualization, Methodology, Software, Validation, Formal analysis, Investigation, Data curation, Writing - Original Draft, Visualization;

**Michele Battistoni:** Conceptualization, Methodology, Validation, Formal analysis, Investigation, Resources, Writing - Review & Editing, Supervision, Project administration;

**Suresh Kumar Nambully:** Conceptualization, Software, Formal analysis, Writing - Review & Editing;

**Adrian Pandal:** Formal analysis, Writing - Review & Editing;

**Cédric Mehl:** Methodology, Software, Validation, Writing - Review & Editing;

**Olivier Colin:** Methodology, Software, Validation, Writing - Review & Editing.

## NOMENCLATURE

<b>AMR</b>	Adaptive Mesh Refinement
<b>aTDC</b>	After Top Dead Center
<b>BMEP</b>	Brake Mean Effective Pressure
<b>CAD</b>	Crank Angle Degree
<b>CCV</b>	Cycle-to-Cycle variability
<b>CFD</b>	Computational Fluid Dynamics
<b>CFL</b>	Courant-Friedrichs-Levy number

<b>COV</b>	Coefficient of Variation
<b>DI</b>	Direct Injection
<b>ECFM</b>	Extended Coherent Flame Model
<b>EV</b>	Electric Vehicle
<b>HCCI</b>	Homogeneous Charge Compression Ignition
<b>HEV</b>	Hybrid Electric Vehicle
<b>ICE</b>	Internal Combustion Engine
<b>IMEP</b>	Indicated Mean Effective Pressure
<b>IT</b>	Ignition Timing
<b>LES</b>	Large-Eddy Simulation
<b>MON</b>	Motor Octane Number
<b>PDF</b>	Probability Density Function
<b>PFI</b>	Port Fuel Injection
<b>PISO</b>	Pressure Implicit with Splitting of Operators
<b>PRF</b>	Primary Reference Fuel
<b>RCCI</b>	Reactivity Controlled Compression Ignition
<b>RON</b>	Research Octane Number
<b>rpm</b>	Revolutions Per Minute
<b>SGS</b>	Subgrid-scale
<b>SI</b>	Spark Ignition
<b>TFM</b>	Thickened Flame Model

## REFERENCES

1. Reitz RD, Ogawa H, Payri R, et al. IJER editorial: The future of the internal combustion engine. *International Journal of Engine Research* 2020, 21(1), 3-10. DOI: <http://doi.org/10.1177/1468087419877990>.
2. Barkenbus JN. Prospects for Electric Vehicles, *Sustainability* 2020, 12(14), 5813. DOI: <https://doi.org/10.3390/su12145813>.
3. Agrawal M, Rajapatel MS. Global Perspective on Electric Vehicle 2020. *International Journal of Engineering Research & Technology* 2020, Vol. 09, 01. DOI: <http://dx.doi.org/10.17577/IJERTV9IS010005>.
4. Leach F, Kalghatgi G, Stone R, et al. The scope for improving the efficiency and environmental impact of internal combustion engines. *Transportation Engineering* 2020, Volume 1, 100005. DOI: <https://doi.org/10.1016/j.treng.2020.100005>.
5. Lecointe B, Monnier G. Downsizing a gasoline engine using turbocharging with direct injection. *SAE Technical Paper* 2003; 2003-01-0542. DOI: <https://doi.org/10.4271/2003-01-0542>.
6. Leach F, Stone R, Richardson D, et al. Particulate Emissions from a Highly Boosted Gasoline Direct Injection Engine. *International Journal of Engine Research* 2018, 19(3), 347-359. DOI: <https://doi.org/10.1177/1468087417710583>.

7. Dong S, Wang Z, Yang C, et al. Investigations on the effects of fuel stratification on auto-ignition and combustion process of an ethanol/diesel dual-fuel engine. *Applied Energy* 2018; 230:19–30. DOI: <https://doi.org/10.1016/j.apenergy.2018.08.082>.
8. Costa M, Catapano F, Sementa P, et al. Mixture preparation and combustion in a GDI engine under stoichiometric or lean charge: an experimental and numerical study on an optically accessible engine. *Applied Energy* 2016; 180:86–103. DOI: <https://doi.org/10.1016/j.apenergy.2016.07.089>.
9. Pan J, Wei H, Shu G, et al. LES analysis for auto-ignition induced abnormal combustion based on a downsized SI engine. *Applied Energy* 2017; 191:183–92. DOI: <https://doi.org/10.1016/j.apenergy.2017.01.044>.
10. Battistoni M, Grimaldi C, Cruccolini V, et al. Assessment of Port Water Injection Strategies to Control Knock in a GDI Engine through Multi-Cycle CFD Simulations. *SAE Technical Paper* 2017; 2017-24-0034. DOI: <https://doi.org/10.4271/2017-24-0034>.
11. Hoppe F, Thewes M, Baumgarten H, et al. Water injection for gasoline engines: Potentials, challenges, and solutions. *International Journal of Engine Research* 2016, 17, 86–96. DOI: <https://doi.org/10.1177/1468087415599867>.
12. Golzari R, Zhao H, Hall J, et al. Impact of intake port injection of water on boosted downsized gasoline direct injection engine combustion, efficiency and emissions. *International Journal of Engine Research* 2021, 22(1), 295-315. DOI: <https://doi.org/10.1177/1468087419832791>.
13. Raut AA, Mallikarjuna JM. Effects of direct water injection and injector configurations on performance and emission characteristics of a gasoline direct injection engine: A computational fluid dynamics analysis. *International Journal of Engine Research* 2020, 21(8), 1520-1540. DOI: <https://doi.org/10.1177/1468087419890418>.
14. Zembi J, Battistoni M, Ranuzzi F, et al. CFD Analysis of Port Water Injection in a GDI Engine under Incipient Knock Conditions. *Energies* 2019, 12, 3409; DOI: <https://doi.org/10.3390/en12183409>.
15. Galloni E, Fontana G, Palmaccio R. Effects of exhaust gas recycle in a downsized gasoline engine. *Applied Energy* 2013; 105:99–107. DOI: <https://doi.org/10.1016/j.apenergy.2012.12.046>.
16. Maldonado BP, Li N, Kolmanovsky I, et al. Learning reference governor for cycle-to-cycle combustion control with misfire avoidance in spark-ignition engines at high exhaust gas recirculation–diluted conditions. *International Journal of Engine Research* 2020, 21(10), 1819-1834. DOI: <https://doi.org/10.1177/1468087420929109>.
17. Ju Y, Sun W. Plasma assisted combustion: Progress, challenges, and opportunities. *Combustion and Flame* 2015, 162, 529–32. DOI: <https://doi.org/10.1016/j.combustflame.2015.01.017>.
18. Marko F, König G, Schöffler T, et al. Comparative Optical and Thermodynamic Investigations of High Frequency Corona- and Spark-Ignition on a CV Natural Gas Research Engine Operated with Charge Dilution by Exhaust Gas Recirculation. *Ignition Systems for Gasoline Engines*, Springer International Publishing 2017, p. 293–314. DOI: [https://doi.org/10.1007/978-3-319-45504-4\\_18](https://doi.org/10.1007/978-3-319-45504-4_18).
19. Tolou S, Schock H. Experiments and modeling of a dual-mode, turbulent jet ignition engine. *International Journal of Engine Research* 2020, 21(6), 966-986. DOI: <https://doi.org/10.1177/1468087419875880>.
20. Bunce M, Cairns A, Blaxill H. The use of active jet ignition to overcome traditional challenges of pre-chamber combustors under low load conditions. *International Journal of Engine Research*, November 2020. DOI: <https://doi.org/10.1177/1468087420972555>.
21. Desantes JM, López JJ, Novella R, et al. Pre-chamber ignition systems: A methodological proposal to reproduce a reference case in a simplified experimental facility for fundamental studies. *International Journal of Engine Research*, November 2020. DOI: <https://doi.org/10.1177/1468087420971115>.
22. Maurya RK, Agarwal AK. Experimental investigation on the effect of intake air temperature and air-fuel ratio on cycle-to-cycle variations of HCCI combustion and performance parameters. *Applied Energy* 2011; 88(4):1153–63. DOI: <https://doi.org/10.1016/j.apenergy.2010.09.027>.
23. Sofianopoulos A, Rahimi Boldaji M, Lawler B, et al. Effect of engine size, speed, and dilution method on thermal stratification of premixed homogeneous charge compression–ignition engines: a large eddy simulation study. *International Journal of Engine Research* 2020, 21(9), 1612-1630. DOI: <https://doi.org/10.1177/1468087418820735>.
24. Kokjohn SL, Hanson RM, Splitter DA, et al. Fuel reactivity controlled compression ignition (RCCI): a pathway to controlled high-efficiency clean combustion. *International Journal of Engine Research* 2011; 12(3):209–26. DOI: <https://doi.org/10.1177/1468087411401548>.

25. Reitz R, Duraisamy G. Review of high efficiency and clean reactivity-controlled compression ignition (RCCI) combustion in internal combustion engines. *Progress in Energy and Combustion Science* 2015; 46:12–71. DOI: <https://doi.org/10.1016/j.pecs.2014.05.003>.
26. Fansler T, Reuss D, Sick V, et al. Invited review: combustion instability in spray guided stratified-charge engines: a review. *International Journal of Engine Research* 2015; 16:260–305. DOI: <https://doi.org/10.1177/1468087414565675>.
27. Gheorghiu V. Ultra-downsizing of internal combustion engines. *Sustainable automotive technologies*. Berlin, Heidelberg: Springer; 2012. DOI: [https://doi.org/10.1007/978-3-642-24145-1\\_20](https://doi.org/10.1007/978-3-642-24145-1_20).
28. Zhao H. HCCI and CAI engines for the automotive industry. *Woodhead Publishing in Mechanical Engineering Series*. Boca Raton, FL/Woodhead, Cambridge, UK: CRC Press; 2007.
29. Pera C, Knop V, Reveillon J. Influence of flow and ignition fluctuations on cycle-to-cycle variations in early flame kernel growth. *Proceedings of the Combustion Institute* 35 (2015) 2897–2905. DOI: <https://doi.org/10.1016/j.proci.2014.07.037>.
30. Ameen M M, Yang X, Kuo T-W, et al. Parallel methodology to capture cyclic variability in motored engines. *International Journal of Engine Research*, 18 (4) 366–377. DOI: <https://doi.org/10.1177/1468087416662544>.
31. Ozdor N, Dulger M, Sher E. Cyclic Variability in Spark Ignition Engines A Literature Survey. *SAE Technical Paper* 940987. DOI: <https://doi.org/10.4271/940987>.
32. Aleiferis P, Hardalupas Y, Taylor A, et al. Flame chemiluminescence studies of cyclic combustion variations and air-to-fuel ratio of the reacting mixture in a lean-burn stratified-charge spark-ignition engine. *Combustion and Flame* 136 (2004) 72–90. DOI: <https://doi.org/10.1016/j.combustflame.2003.09.004>.
33. Dreher D, Schmidt M, Welch C, et al. Deep feature learning of in-cylinder flow fields to analyze cycle-to-cycle variations in an SI engine. *International Journal of Engine Research*, December 2020. DOI: <https://doi.org/10.1177/1468087420974148>.
34. Pera C, Chevillard S, Reveillon J. Effects of residual burnt gas heterogeneity on early flame propagation and on cyclic variability in spark-ignited engines. *Combustion and Flame* 160 (2013) 1020–1032. DOI: <https://doi.org/10.1016/j.combustflame.2013.01.009>.
35. Burluka A, Hussin A.E.-D, Ling Z. Effects of large-scale turbulence on cyclic variability in spark-ignition engine. *Experimental Thermal and Fluid Science* 43 (2012) 13–22. DOI: <https://doi.org/10.1016/j.expthermflusci.2012.04.012>.
36. Vermorel O, Richard S, Colin O, et al. Multi-Cycle LES Simulations of Flow and Combustion in a PFI SI 4-Valve Production Engine. *SAE Technical Paper* 2007, 2007-01-0151. DOI: <https://doi.org/10.4271/2007-01-0151>.
37. Goryntsev D, Sadiki A, Klein M, et al. Large Eddy Simulation based analysis of the effects of cycle-to-cycle variations on air-fuel mixing in realistic DISI IC engines. *Proceedings of the Combustion Institute* 32, 2759-2766 (2009). DOI: <https://doi.org/10.1016/j.proci.2008.06.185>.
38. Hasse C, Sohm V, Durst B. Numerical investigation of cyclic variations in gasoline engines using a hybrid URANS/LES modeling approach. *Computers & Fluids* 39 (1) 25-48 (2010). DOI: <https://doi.org/10.1016/j.compfluid.2009.07.001>.
39. Zembi J, Mariani F, Battistoni M. Large Eddy Simulation of Ignition and Combustion Stability in a Lean SI Optical Access Engine. *SAE Technical Paper* 2019, 2019-24-0087. DOI: <https://doi.org/10.4271/2019-24-0087>.
40. Netzer C, Seidel L, Ravet F, et al. Assessment of the validity of RANS knock prediction using the resonance theory. *International Journal of Engine Research* 2020, 21(4), 610-621. DOI: <https://doi.org/10.1177/1468087419846032>.
41. Vermorel O, Richard S, Colin O, et al. Towards the understanding of cyclic variability in a spark ignited engine using multi-cycle LES. *Combustion and Flame* 156, 1525-1541 (2009). DOI: <https://doi.org/10.1016/j.combustflame.2009.04.007>.
42. Richard S, Colin O, Angelberger C. Towards large eddy simulation of combustion in spark ignition engines. *Proceedings of the Combustion Institute* 31 (2007) 3059–3066. DOI: <https://doi.org/10.1016/j.proci.2006.07.086>.
43. Granet V, Vermorel O, Lacour C, et al. Large-eddy simulation and experimental study of cycle-to-cycle variations of stable and unstable operating points in a spark ignition engine. *Combustion and Flame* 159(4) (2012) 1562–1575. DOI: <https://doi.org/10.1016/j.combustflame.2011.11.018>.

44. Enaux B, Granet V, Vermorel O, et al. LES and experimental study of cycle-to-cycle variations in a spark ignition engine. *Proceedings of the Combustion Institute* 33, 3115-3122 (2011). DOI: <https://doi.org/10.1016/j.proci.2010.07.038>.
45. Banaeizadeh A, Afshari A, Schock H, et al. Large-eddy simulations of turbulent flows in internal combustion engines. *International Journal of Heat and Mass Transfer* 60 (2012) 781–796. DOI: <https://doi.org/10.1016/j.ijheatmasstransfer.2012.12.065>.
46. Huijnen V, Somers L, Baert R. Study of turbulent flow structures of a practical-steady engine head flow using large-eddy simulations. *Journal of Fluids Engineering* 128 (6) (2006) 1181–1191. DOI: <https://doi.org/10.1115/1.2353259>.
47. Celik I, Yavuz I, Smirnov A, et al. Prediction of in-cylinder turbulence for IC engines. *Combustion Science and Technology* 153(1):339-368. DOI: <https://doi.org/10.1080/00102200008947269>.
48. Haworth D. Large eddy simulation of in-cylinder flows. *Oil and Gas Science and Technology Rev. IFP* 54 (2) (1999) 175–185. DOI: <https://doi.org/10.2516/ogst:1999012>.
49. Tatschl R, Bogensperger M, Pavlovic Z, et al. Les simulation of flame propagation in a direct-injection SI-engine to identify the causes of cycle-to-cycle combustion variations. *SAE Technical Paper* 2013, 2013-01-1084. DOI: <https://doi.org/10.4271/2013-01-1084>.
50. Goryntsev D, Sadiki A, Janicka J. Analysis of misfire processes in realistic direct injection spark ignition engine using multi-cycle large eddy simulation. *Proceedings of the Combustion Institute* 34 (2) (2013) 2969–2976. DOI: <https://doi.org/10.1016/j.proci.2012.08.011>.
51. Drake M, Haworth D. Advanced gasoline engine development using optical diagnostics and numerical modeling. *Proceedings of the Combustion Institute* 31 (2007) 99–124. DOI: <https://doi.org/10.1016/j.proci.2006.08.120>.
52. Su Y, Splitter D, Kim SH. Laminar-to-turbulent flame transition and cycle-to-cycle variations in large eddy simulation of spark-ignition engines. *International Journal of Engine Research*, October 2020. DOI: <https://doi.org/10.1177/1468087420962346>.
53. Truffin K, Angelberger C, Richard S, et al. Using large-eddy simulation and multivariate analysis to understand the sources of combustion cyclic variability in a spark-ignition engine. *Combustion and Flame* 162 (2015) 4371–4390. DOI: <https://doi.org/10.1016/j.combustflame.2015.07.003>.
54. Thobois L, Lauvergne R, Poinot T. Using LES to investigate reacting flow physics in engine design process. *SAE Technical Paper* 2007, 2007-01-0166. DOI: <https://doi.org/10.4271/2007-01-0166>.
55. Colin O, Ducros F, Veynante D, et al. A thickened flame model for large eddy simulations of turbulent premixed combustion. *Physics of Fluids*, Vol. 12, No. 7, 2000, pp. 1843–1863. DOI: <https://doi.org/10.1063/1.870436>.
56. Candel S M, Poinot T. Flame stretch and the balance equation for the flame surface area. *Combustion Science and Technology* 70(1-3):1-15. DOI: <https://doi.org/10.1080/00102209008951608>.
57. Colin O, Benkenida A, Angelberger C. 3D modeling of mixing, ignition and combustion phenomena in highly stratified gasoline engine. *Oil and Gas Science and Technology* 58(1):47-62. DOI: <https://doi.org/10.2516/ogst:2003004>.
58. Fontanesi S, Paltrinieri S, Tiberi A, et al. LES multi-cycle analysis of a high performance GDI engine. *SAE Technical Paper* 2013, 2013-01-1080. DOI: <https://doi.org/10.4271/2013-01-1080>.
59. Rulli F, Barbato A, Fontanesi S, d’Adamo A. Large eddy simulation analysis of the turbulent flow in an optically accessible internal combustion engine using the overset mesh technique. *International Journal of Engine Research*, January 2020. DOI: <https://doi.org/10.1177/1468087419896469>.
60. Zhao L, Moiz A, Som S, et al. Examining the role of flame topologies and in-cylinder flow fields on cyclic variability in spark-ignited engines using large-eddy simulation. *International Journal of Engine Research* 1–19. DOI: <https://doi.org/10.1177/1468087417732447>.
61. Charlette F, Meneveau C, Veynante D. A power-law flame wrinkling model for LES of premixed turbulent combustion Part I: non-dynamic formulation and initial tests. *Combustion and Flame* Vol. 131, No. 1, 2002, pp. 159–180. DOI: [https://doi.org/10.1016/S0010-2180\(02\)00400-5](https://doi.org/10.1016/S0010-2180(02)00400-5).
62. Volpiani P S, Schmitt T, Veynante D. Large eddy simulation of a turbulent swirling premixed flame coupling the TFLES model with a dynamic wrinkling formulation. *Combustion and Flame* Vol. 180, 2017, pp. 124–135. DOI: <https://doi.org/10.1016/j.combustflame.2017.02.028>.
63. Mehl C, Liu S, See Y C, et al. LES of a stratified turbulent burner with a Thickened Flame Model coupled to Adaptive Mesh Refinement and detailed chemistry. *2018 Joint Propulsion Conference*. DOI: <https://doi.org/10.2514/6.2018-4563>.

64. Donadio G, Poggiani C, Rondoni L, et al. Combustion Analysis in an Optical Access Engine. *Energy Procedia* 45:959-966, 2014. DOI: <https://doi.org/10.1016/j.egypro.2014.01.101>.
65. Ricci F, Zembi J, Battistoni M, et al. Experimental and Numerical Investigations of the Early Flame Development Produced by a Corona Igniter. *SAE Technical Paper* 2019, 2019-24-0231. DOI: <https://doi.org/10.4271/2019-24-0231>.
66. Battistoni M, Mariani F, Risi F, et al. Combustion CFD Modeling of a Spark Ignited Optical Access Engine Fueled with Gasoline and Ethanol. *Energy Procedia* 82:424-431, 2015. DOI: <https://doi.org/10.1016/j.egypro.2015.11.829>.
67. Cimarello A, Grimaldi C N, Mariani F, et al. Analysis of RF Corona Ignition in Lean Operating Conditions Using an Optical Access Engine, *SAE Technical Paper* 2017, 2017-24-0673. DOI: <https://doi.org/10.4271/2017-01-0673>.
68. Cimarello A, Cruccolini V, Discepoli G, et al. Combustion Behavior of an RF Corona Ignition System with Different Control Strategies, *SAE Technical Paper* 2018, 2018-01-1132. DOI: <https://doi.org/10.4271/2018-01-1132>.
69. Richards K J, Senecal P K, Pomraning E. CONVERGE 3.0, Convergent Science, Madison, WI (2020).
70. Senecal P, Richards K, Pomraning E, et al. A New Parallel Cut-Cell Cartesian CFD Code for Rapid Grid Generation Applied to in-Cylinder Diesel Engine Simulations, *SAE Technical Paper* 2007, 2007-01-0159. DOI: <https://doi.org/10.4271/2007-01-0159>.
71. Issa R I. Solution of the Implicitly Discretised Fluid Flow Equations by Operator-Splitting. *Journal of Computational Physics*, 62(1), 40-65, 1986. DOI: [https://doi.org/10.1016/0021-9991\(86\)90099-9](https://doi.org/10.1016/0021-9991(86)90099-9).
72. Pomraning E. Development of Large Eddy Simulation Turbulence Models. Ph.D. Thesis, University of Wisconsin-Madison, Madison, WI, 2000.
73. Givler S, Raju M, Pomraning E, et al. Gasoline Combustion Modeling of Direct and Port-Fuel Injected Engines using a Reduced Chemical Mechanism. *SAE Technical Paper* 2013, 2013-01-1098. DOI: <https://doi.org/10.4271/2013-01-1098>.
74. Richard S, Dulbecco A, Angelberger C, et al. Invited Review: Development of a one-dimensional computational fluid dynamics modeling approach to predict cycle-to-cycle variability in spark-ignition engines based on physical understanding acquired from large-eddy simulation. *International Journal of Engine Research* 2015, 16(3), 379-402. DOI: <https://doi.org/10.1177/1468087414560592>.
75. Discepoli G, Cruccolini V, Dal Re M, et al. Experimental Assessment of Spark and Corona Igniters Energy Release. *Energy Procedia* 148: 1262-1269, 2018. DOI: <https://doi.org/10.1016/j.egypro.2018.08.001>.
76. O'Rourke P J, Bracco F V. Two scaling transformations for the numerical computation of multidimensional unsteady laminar flames. *Journal of Computational Physics*, Vol. 33, No. 2, 1979, pp. 185–203. DOI: [https://doi.org/10.1016/0021-9991\(79\)90015-9](https://doi.org/10.1016/0021-9991(79)90015-9).
77. Butler T, O'Rourke P J. A numerical method for two dimensional unsteady reacting flows. *Symposium on Combustion*, Vol. 16, No. 1, 1977, pp. 1503–1515. DOI: [https://doi.org/10.1016/S0082-0784\(77\)80432-3](https://doi.org/10.1016/S0082-0784(77)80432-3).
78. Legier J P, Poinot T, Veynante D. Dynamically thickened flame LES model for premixed and non-premixed turbulent combustion. *Proceedings of the Summer Program, Center for Turbulence Research*, 2000, pp. 157–168.
79. Jaravel T. Prediction of pollutants in gas turbines using Large Eddy Simulation. Ph.D. Thesis, CERFACS, 2016.
80. Matekunas F. Modes and measures of cyclic combustion variability. *SAE Technical Paper* 830337; 1983. DOI: <https://doi.org/10.4271/830337>.
81. Charlette F, Meneveau C, Veynante D. A power-law flame wrinkling model for LES of premixed turbulent combustion Part II: dynamic formulation. *Combustion and Flame* Vol. 131, No. 1, 2002, pp. 181–197. DOI: [https://doi.org/10.1016/S0010-2180\(02\)00401-7](https://doi.org/10.1016/S0010-2180(02)00401-7).
82. Mouriaux S, Colin O, Veynante D. Adaptation of a dynamic wrinkling model to an engine configuration. *Proceedings of the Combustion Institute* Vol. 36, No. 3, 2017, pp. 3415-3422. DOI: <https://doi.org/10.1016/j.proci.2016.08.001>.